UNIVERSIDAD DE CONCEPCIÓN

Centro de Investigación en Ingeniería Matemática (CI^{2}MA)

A multilayer shallow water model for tsunamis and coastal forest interaction

Raimund Bürger, Enrique D. Fernández Nieto, Jorge Moya

PREPRINT 2024-07

SERIE DE PRE-PUBLICACIONES

e-mail: rburger@ing-mat.udec.cl e-mail: edofer@us.es e-mail: jorgemoya@udec.cl

A MULTILAYER SHALLOW WATER MODEL FOR TSUNAMIS AND COASTAL FOREST INTERACTION *, **, ***

Raimund Burger[1], Enrique D. Fernandez-Nieto[2] and Jorge Moya[1]

Abstract. Models and numerical methods of the impact of tsunamis on coastal forests are of vital importance for exploring the potential of coastal vegetation as a means of mitigation. Such a model is formulated as a multilayer shallow water system based on a free-surface formulation of the Euler equations for an ideal fluid. Specifically, the Euler equations are approximated by a layer averaged non-hydrostatic (LDNH) approach involving linear pressures and piecewise constant velocities. Furthermore, based on [K. Iimura and N. Tanaka, Numerical simulation estimating effects of tree density distribution in coastal forest on tsunami mitigation, *Ocean Engrg.* **54** (2012) 223–232] drag forces, inertia forces, and porosity are added to model the interaction with the forest. These ingredients are specified in a layer-wise manner. Thus, the vertical features of the forest are described with higher accuracy than within a single-layer approach. Projection methods for the non-hydrostatic pressure in conjunction with polynomial viscosity matrix finite volume methods [M. J. Castro and E. Fernández-Nieto, A class of computationally fast first order finite volume solvers: PVM methods. *SIAM J. Sci. Comput.* **34** (2012) A2173–A2196] are employed for the numerical solution of the multilayer model, that is for the propagation of tsunamis and coastal flooding. Experimental observations and field data are used to validate the model. In general good agreement is obtained. Results indicate, moreover, that coastal vegetation can operate as an efficient natural barrier against coastal hazards and can significantly reduce the effects of tsunamis.

2020 Mathematics Subject Classification. 65M06, 76D99.

.

Keywords and phrases: finite volume method, layer averaged non-hydrostatic approach, multilayer model, coastal forest, tsunami mitigation

* *R.B. is supported by ANID (Chile) through Fondecyt project 1210610, Anillo ANID/ACT210030, Centro de Modelamiento Matemático CMM (BASAL project FB210005), and CRHIAM, projects ANID/FONDAP/15130015 and ANID/ FONDAP/1523A0001.*

** *E.F.N. is supported by the Spanish Government and FEDER through the research project PID2022-137637NB-C22 and the regional Andalusian Government I+D+i PAIDI 2021 project ProyExcel_00525.*

*** *J.M. supported by ANID scholarship ANID-PCHA/Doctorado Nacional/2021-21211457 and the regional Andalusian Government I+D+i PAIDI 2021 project ProyExcel_00525.*

[1] CI[2]MA and Departamento de Ingeniería Matemática, Facultad de Ciencias Físicas y Matemáticas, Universidad de Concepción, Casilla 160-C, Concepción, Chile.

[2] Departamento de Matemática Aplicada I, ETS Arquitectura, Universidad de Sevilla, Avda. Reina Mercedes No. 2, 41012 Sevilla, Spain.

1. Introduction

1.1. Scope

A number of geophysical applications such as shallow water flows, free surface flows, gravity currents, sediment transport and avalanches give rise to a system of first-order partial differential equations (PDEs) in the vectorial form

$$\partial_t \boldsymbol{W} + \partial_x \boldsymbol{F}(\boldsymbol{W}) + \boldsymbol{B}(\boldsymbol{W})\partial_x \boldsymbol{W} = \boldsymbol{S}(\boldsymbol{W})\sigma'(x), \tag{1}$$

where t is time, x is the spatial coordinate, and the sought quantity is a vector $\boldsymbol{W} = \boldsymbol{W}(x,t)$ of state variables, where $\boldsymbol{W}$ belongs to an open convex subset $D \subseteq \mathbb{R}^{\mathcal{N}}$. The vector functions $\boldsymbol{F} : D \to \mathbb{R}^{\mathcal{N}}$ and $\boldsymbol{S} : D \to \mathbb{R}^{\mathcal{N}}$ as well as the matrix function $\boldsymbol{B} : D \to \mathbb{R}^{\mathcal{N}\times\mathcal{N}}$ and the real scalar function $\sigma = \sigma(x)$ are given. Solutions of equations of this type are in general discontinuous, and the well-known salient property of the system (1) that complicates its analytical and numerical treatment is the presence of nonconservative products such as $\boldsymbol{B}(\boldsymbol{W})\partial_x \boldsymbol{W}$ [10, 12].

It is the purpose of this contribution to study a specific model of the form (1) that arises as a multilayer shallow water system based on a free-surface formulation of the Euler equations for an ideal fluid. Specifically, the Euler equations are approximated by a layer-averaged non-hydrostatic (LDNH) approach involving linear pressures, piecewise constant horizontal velocities and piecewise linear vertical velocities. Furthermore, specific ingredients such as drag forces, inertia forces, and porosity are adopted from the literature of ocean engineering, landscape ecology and related fields [19,24,29,30,32] and are incorporated to form a new model of the interaction of a tsunami wave with a coastal forest. In fact, such models and numerical methods are of vital importance for exploring the potential of coastal vegetation as a means of mitigation. A particular feature of the present approach is the description of tree-specific ingredients in a layer-wise manner. Thus, the vertical features of the forest are described with higher accuracy than within a single-layer approach. Projection methods for the non-hydrostatic pressure in conjunction with polynomial viscosity matrix finite volume methods [8] are employed for the numerical solution of the multilayer model, that is for the propagation of tsunamis and coastal flooding. Experimental observations and field data are used to validate the model.

1.2. Related work

Finite volume (FV) schemes are a standard method for solving hyperbolic systems of partial differential equations (PDEs). However, hyperbolic systems arising from balance equations in geophysical applications usually involve nonconservative products that complicate the application of traditional FV schemes. The standard example are shallow water equations with variable bottom topography. A well-known class of FV schemes that can handle nonconservative products are the so-called path-conservative schemes [11, 21, 31]. These schemes are designed specifically for nonconservative systems and are based on the concept of path integration. Path-conservative schemes have been applied to a variety of hyperbolic systems with nonconservative products, including two-layer and layer-averaged shallow water equations, compressible gas dynamics and magnetohydrodynamics. In [22] a generalization of the Roe method [25] was proposed (see also [31]). Nevertheless, its implementation requires explicit knowledge of the eigenstructure of the intermediate matrices. In [8] a specific family of path-conservative schemes is proposed, named polynomial viscosity matrix methods (PVM methods) that generalized several incomplete Riemann solvers such as Rusanov, Lax-Friedrichs or HLL, among others.

Multilayer models are designed to avoid solving a fully three-dimensional model (such as the Navier–Stokes equations for an incompressible fluid). They are based on the so-called shallow water or Saint-Venant approach, that is, a vertically integrated version of the underlying model [1–7, 14, 16, 26], in our case the Euler equations for an ideal fluid. The multilayer approach consists in subdividing the computational domain into N layers in the vertical direction, which leads to a system of Saint-Venant equations. The unknowns in the present case are horizontal velocities by layer, the total height of the fluid column, and pressure.

The present approach is based on the LDNH_0 model with non-hydrostatic pressure. this approach as an improvement compared with standard shallow-water-based models since the latter usually only cover hydrostatic pressures and neglect vertical acceleration (and therefore dispersive) effects. On the other hand, dispersive

models like Boussinesq introduce high-order derivatives for the unknowns, while the LDNH_0 model incorporates these dispersive effects into the non-hydrostatic pressure terms [13, 17].

From the applicative point of view, the general significance of tsumami disaster mitigation by the natural method of coastal forest plantation is discussed in the overview article by Tanaka [30] (for instance). The present work is based on technically more detailed information provided in [19, 24, 28, 29, 32].

1.3. **Outline of the paper**

The remainder of the paper is organized as follows. In Section 1 we introduce preliminaries, starting with the basic method for the discretization of (1). In Sections 1.2 and 1.3 we study properties the numerical methods need to have in order to be well balanced and behave correctly in dry front situations. To put the LDNH_0 approach into the proper perspective we first formulate, in Section 1.4, a hydrostatic reconstruction of a two-equation shallow water model with a source term, and then, based on these results, we proceed in Section 1.5 to formulate the linearized discontinuous non-hydrostatic model (LDNH_0 model) whose unknowns are the height of the water level, the horizontal and the vertical velocity, and pressure as functions of position x and time t. The first three of these quantities are specified by a first-order system of balance laws that in each time step can be handled by the same discretization as the shallow water equations along with hydrostatic reconstruction. The non-hydrostatic pressure, in turn, is updated via a projection step. Finally, we specify in Section 1.6 the inertia and drag forces related to the coastal forest along with the corresponding concept of porosity. The result is the non-hydrostatic LDNH_0 model, specified for forest forces, in final form. Section 2 is devoted to the development of the discretization of the LDNH_0 model. To this end we formulate first, in Section 2.1, a preliminary discretization of the first step of Section 1.5 that excludes the non-hydrostatic pressure terms which are handled by the projection method. This preliminary discretization is based on plausible arguments but turned out to be unstable due to the nature of the inertia force. An alternative, slightly different but stable discretization is advanced in Section 2.2. The numerical method relies on knowledge of the eigenvalues of a matrix related to the Jacobian matrix of the system. These eigenvalues are obtained in Section 2.3. Finally, in Section 2.4 the scheme that discretizes the elliptic problem for the pressure update is formulated. The treatment of Section 2 refers to the single-layer LDNH_0 model. The multilayer version of that model and its discretization are described in in Section 3, starting with the definition of multiple layers (Section 3.1). We then present (in Section 3.2) the LDNH_0 multilayer model (without forces and porosity) arising from layer-wise vertical integration. After discussing layer-wise porosity (in Section 3.3) we derive in Section 3.4 explicit expressions of the interlayer transfer terms. We then formulate ingredients of the multilayer model that are specific to the application to a forest, namely drag and inertia forces, friction, and viscosity (Sections 3.5 and 3.6). The resulting multilayer model is summarized in Section 3.7. Next, we outline the discretization of the multilayer model. Roughly speaking, the discretization of the first-order system, described in Section 3.8, is a multilayer version of the discretization of Section 2.2 for the single-layer case (in both cases, non-hydrostatic pressure is disregarded). The remaining ingredients of the multilayer scheme, namely the projection matrix describing the solution of the elliptic problem for the pressure update and finally, the interlayer viscosity effect, are described in Sections 3.9 and 3.10, respectively. Section 4 is devoted to the presentation of numerical examples. To test the accuracy of the scheme we consider in Example 1 (Section 4.1) the exact soliton solution of the LDNH_0 soliton (described in Appendix A). Examples 2 to 6 are motivated by selected experiments conducted by Iimura and Tanaka [19]. They are solved in Section 4.1 by the single-layer LDNH_0 test model. Examples 7 to 10 are related test cases but with limited tree height, and Examples 11 to 15 consider trees with properties that gradually vary with height. These cases are solved by the multilayer LDNH_0 model in Sections 4.2 and 4.3. An alternative approach to specify the drag, namely to specify the drag by a suitable Reynolds number, is discussed in Section 4.4. Finally, in Section 5 we examine possible directions for future research and address the results of the study. The practical implications of the model for environmental conservation, disaster resilience, and coastal design are discussed in this work.

2. Preliminaries

2.1. **Basic method**

Let us consider a uniform mesh of cells $I_i = [x_{i-1/2}, x_{i+1/2}]$, where $x_i = i\Delta x$, $i \in \mathbb{Z}$, and time steps $t_\nu = \nu\Delta t$, $\nu \in \mathbb{N}_0$. Then a first-order finite volume discretization of (1) can be written as

$$\boldsymbol{W}_i^{\nu+1} = \boldsymbol{W}_i^{\nu} - \frac{\Delta t}{\Delta x}(\boldsymbol{D}_{i-1/2}^{\nu,+} + \boldsymbol{D}_{i+1/2}^{\nu,-}), \quad i \in \mathbb{Z}, \quad \nu \in \mathbb{N}_0 \tag{2}$$

(see [8] for details), where we define the numerical flux vectors

$$\begin{aligned}\boldsymbol{D}_{i+1/2}^{\nu,\pm} = \frac{1}{2}(\boldsymbol{F}(\boldsymbol{W}_{i+1}^{\nu}) - \boldsymbol{F}(\boldsymbol{W}_i^{\nu}) + \boldsymbol{\mathcal{B}}_{i+1/2}^{\nu}(\boldsymbol{W}_{i+1}^{\nu} - \boldsymbol{W}_i^{\nu}) - (\sigma_{i+1} - \sigma_i)\boldsymbol{\mathcal{S}}_{i+1/2}^{\nu} \\ \pm \boldsymbol{Q}_{i+1/2}^{\nu}(\boldsymbol{W}_{i+1}^{\nu} - \boldsymbol{W}_i^{\nu} - (\sigma_{i+1} - \sigma_i)(\boldsymbol{\mathcal{A}}_{i+1/2}^{\nu})^{-1}\boldsymbol{\mathcal{S}}_{i+1/2}^{\nu})),\end{aligned} \tag{3}$$

where $\boldsymbol{Q}_{i+1/2}^{\nu}$ is a numerical viscosity matrix, $\boldsymbol{\mathcal{B}}_{i+1/2}^{\nu}$ and $\boldsymbol{\mathcal{A}}_{i+1/2}^{\nu}$ are intermediate matrices, and $\boldsymbol{\mathcal{S}}_{i+1/2}^{\nu}$ is the intermediate vector, corresponding to the states $\boldsymbol{W}_{i+1/2}^{\nu,-}$ and $\boldsymbol{W}_{i+1/2}^{\nu,+}$ of $\boldsymbol{B}$, $\boldsymbol{A}$, and $\boldsymbol{S}$, respectively. The Jacobian matrix of the system (1),

$$\boldsymbol{A} := \frac{\partial \boldsymbol{F}(\boldsymbol{W})}{\partial \boldsymbol{W}} + \boldsymbol{B}(\boldsymbol{W}),$$

encodes the linear relationship between the derivative terms and the unknowns in the system. Notice that the scheme (2) is not conservative. A standard choice of the viscosity matrix is the one that corresponds to the HLL flux [8] given by

$$\boldsymbol{Q}(\boldsymbol{A}) = \alpha_0\boldsymbol{I} + \alpha_1\boldsymbol{A} \quad \text{with} \quad \alpha_0 = \frac{S_{\mathrm{R}}|S_{\mathrm{L}}| - S_{\mathrm{L}}|S_{\mathrm{R}}|}{S_{\mathrm{R}} - S_{\mathrm{L}}}, \quad \alpha_1 = \frac{|S_{\mathrm{R}}| - |S_{\mathrm{L}}|}{S_{\mathrm{R}} - S_{\mathrm{L}}},$$

where $\boldsymbol{I}$ is the $\mathcal{N} \times \mathcal{N}$ identity matrix. If we assume that the eigenvalues $\lambda_{1,i+1/2}, \ldots, \lambda_{\mathcal{N},i+1/2}$ of $\boldsymbol{A}$ are real, then a possible choice for S_{L} and S_{R} is

$$S_{\mathrm{L}} = \min\{\lambda_{1,i+1/2}, \ldots, \lambda_{\mathcal{N},i+1/2}\}, \quad S_{\mathrm{R}} = \max\{\lambda_{1,i+1/2}, \ldots, \lambda_{\mathcal{N},i+1/2}\}.$$

In general S_{R} and S_{L} represent the upper and the lower bound of the region in which the eigenvalues of the system are located.

2.2. **Dry/wet fronts**

The term "dry/wet front" (DWF) is frequently used to address the interface between a region with fluid and a region without fluid. In the case of a tsunami simulation, the DWF describes the interface between the advancing tsunami wave and the dry land. As the wave approaches the coastline, the DWF moves inland, with the speed and behavior of the front affected by a variety of factors, such as the topography and bathymetry of the coastline, and the magnitude and duration of the wave. Accurately modeling the behavior of the DWF is evidently important for predicting the behavior of waves in coastal areas, and for assessing the risk and impact of tsunami events. A correct implementation of this front is crucial to preserve the well-balancing properties of the numerical method, this is, the method should preserve the equilibrium state of the fluid flow, where the water level is constant and the velocity is zero, in the presence of non-uniform bottom topography or other sources of external forces, which is critical for predicting the behavior of waves in coastal areas. In particular, well-balanced methods ensure that the numerical solution accurately captures the location of the DWF and the speed of its movement. Numerical methods that are not well-balanced can produce spurious oscillations or artificial numerical diffusion at the DWF, which can lead to inaccurate simulation results. Such methods can also violate the conservation laws leading to nonphysical solutions.

2.3. **Well-balanced property**

Consider a simple shallow-water system of equations

$$\begin{aligned} \partial_t h + \partial_x q_u &= 0, \\ \partial_t q_u + \partial_x\left(\frac{q_u^2}{h} + \frac{1}{2}gh^2\right) &= -ghz_{\mathrm{b}}'(x), \end{aligned} \tag{4}$$

where h is the water depth, u is the water velocity, $q_u := hu$ and $z_{\mathrm{b}} = z_{\mathrm{b}}(x)$ is the channel bottom with $x \in [0, L]$ and $t \in [0, T]$, see Figure 1 (a). To derive this model, and in general any other Boussinesq system, from the

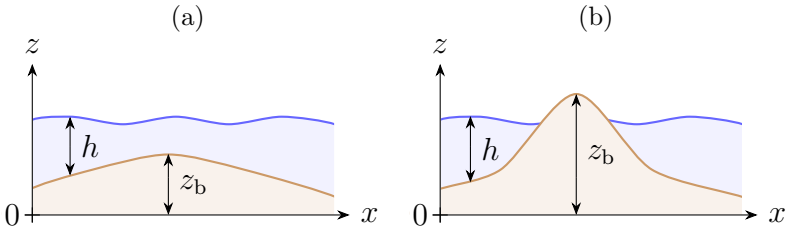

FIGURE 1. Schematic (a) of the physical system, (b) of the physical system with dry fronts.

Navier-Stokes equations it is assumed that $h > 0$. However, this assumption does not allow us, for example, to simulate waves reaching a coast. One needs to extend this kind of model to handle physically correctly situations when $h = 0$. To this end, the definition

$$\eta(x, t) \coloneqq h(x, t) + z_{\mathrm{b}}(x)$$

is very useful since in a steady state, η should be a constant. In fact, for $q_u = 0$ the shallow water system (4) reduces to

$$\partial_t h = 0, \quad gh\partial_x h = -ghz_{\mathrm{b}}' \quad \Rightarrow \quad h = h(x), \quad \partial_x(h + z_{\mathrm{b}}) = 0.$$

To achieve that the numerical scheme does not introduce non-physical oscillations, Castro et al. [9] introduced the following well-balanced condition called "conservation property" or "C-property":

Definition 2.1 (C-property)**.** A numerical scheme is said to *possess the C-property* if it exactly reproduces the steady-state solutions $q_u \equiv 0$, $h \equiv \eta - z_{\mathrm{b}}$, where η is a constant such that $\eta > \max_{x\in[0,L]} z_{\mathrm{b}}(x)$.

Consequently, for model with $h > 0$ a stable numerical scheme should have the C-property to avoid non-physical oscillations. However, this property does not handle the presence of dry fronts. In fact, in the situation of Figure 1 (b) there are regions where $h(x)$ is not well defined, and even if we set $h(x) = 0$ in these regions, the steady state is not satisfied because η in a dry region is higher than in a wet region. To include these cases, Castro et al. defined in [9] the following "extended C-property":

Definition 2.2 (Extended C-property)**.** A numerical scheme is said to have the *extended C-property* if it reproduces exactly the steady-state solutions

$$q_u \equiv 0, \quad h(x) = \begin{cases} \eta - b(x) & \text{if } \eta > z_{\mathrm{b}}(x), \\ 0 & \text{otherwise.} \end{cases}$$

Since h can be zero, we need to renormalize this quantity to avoid dividing by zero (for example in the term q_u^2/h in the second equation of (4)). In general, for a given variable q divided by h the corresponding quotient is approximated by

$$\frac{q}{h} \approx \frac{\sqrt{2}qh}{\sqrt{h^4 + \max\{h^4, \varepsilon^4\}}},$$

where $0 < \varepsilon \ll 1$ a small constant (in general it is chosen as $\varepsilon = 10^{-6}$ or smaller), cf., e.g., [20]. This property is fundamental to correctly describe coastal scenarios. However, shallow water models do in general not have this property but, for the model to be compatible with the extended C-property it must be treated. This treatment will be presented below.

2.4. **Hydrostatic reconstruction**

We rewrite system (4) as

$$\partial_t \boldsymbol{W} + \partial_x \boldsymbol{F}(\boldsymbol{W}) = \boldsymbol{S} z_{\mathrm{b}}',$$

where we define the vectors

$$\boldsymbol{W} \coloneqq \begin{pmatrix} h \\ q_u \end{pmatrix}, \quad \boldsymbol{F}(\boldsymbol{W}) \coloneqq \begin{pmatrix} q_u \\ \dfrac{q_u^2}{h} + \dfrac{gh^2}{2} \end{pmatrix}, \quad \boldsymbol{S} \coloneqq \begin{pmatrix} 0 \\ gh \end{pmatrix}$$

and the matrix of the system, that is, the Jacobian matrix of $\boldsymbol{F}(\boldsymbol{W})$,

$$\boldsymbol{A}(\boldsymbol{W}) = \frac{\partial \boldsymbol{F}(\boldsymbol{W})}{\partial \boldsymbol{W}} = \begin{bmatrix} 0 & 1 \\ gh - \dfrac{q_u^2}{h^2} & 2\dfrac{q_u}{h} \end{bmatrix}$$

that has the eigenvalues

$$\lambda_1 = u - \sqrt{gh}, \quad \lambda_2 = u + \sqrt{gh}.$$

The $\boldsymbol{F}$- and $\boldsymbol{S}$-terms of the numerical flux (3) are given by

$$\begin{aligned} &\boldsymbol{F}(\boldsymbol{W}_{i+1}) - \boldsymbol{F}(\boldsymbol{W}_i) - \frac{1}{2}(\sigma_{i+1} - \sigma_i)(\boldsymbol{S}_{i+1} + \boldsymbol{S}_i) \\ &= \begin{pmatrix} q_{u,i+1}^\nu - q_{u,i}^\nu \\ \dfrac{(q_{u,i+1}^\nu)^2}{h_i^\nu} + g\dfrac{(h_{i+1}^\nu)^2}{2} - \dfrac{(q_{u,i}^\nu)^2}{h_{i-1}^\nu} - g\dfrac{(h_i^\nu)^2}{2} \end{pmatrix} + \begin{pmatrix} 0 \\ \dfrac{g}{2}(h_{i+1}^\nu + h_i^\nu)(z_{\mathrm{b},i+1} - z_{\mathrm{b},i}) \end{pmatrix}. \end{aligned} \tag{5}$$

At steady state, $q_{u,i}^\nu = 0$ for all i, and the second component of (5) becomes

$$\begin{aligned} &\frac{g}{2}((h_{i+1}^\nu)^2 - (h_i^\nu)^2) + \frac{g}{2}((h_{i+1}^\nu + h_i^\nu)(z_{\mathrm{b},i+1} - z_{\mathrm{b},i})) \\ &= \frac{g}{2}(h_{i+1}^\nu - h_i^\nu)(h_{i+1}^\nu + h_i^n) + \frac{g}{2}((h_{i+1}^\nu + h_i^\nu)(z_{\mathrm{b},i+1} - z_{\mathrm{b},i})) \\ &= \frac{g}{2}(h_{i+1}^\nu + h_i^\nu)((h_{i+1}^\nu + z_{\mathrm{b},i+1}) - (h_i^\nu + z_{\mathrm{b},i})). \end{aligned} \tag{6}$$

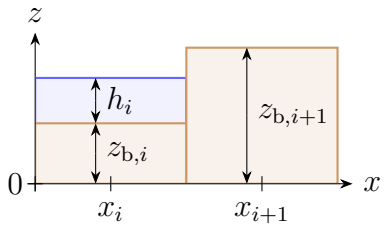

FIGURE 2. Schematic of a dry front.

In absence of dry fronts this last expression is zero because at steady state, $h+z_b$ is constant, but in a system where $h=0$ is allowed, it may occur that, for example, $h_i^\nu > 0$, $h_{i+1}^\nu = 0$, and $h_i < z_{i+1} - z_i$, as is shown in Figure 2. In this case the last expression in (6) reduces to

$$\frac{g}{2} h_i^\nu (z_{b,i+1} - (h_i^\nu + z_{b,i})) < 0;$$

in other words, we will get non-physical velocities that can break our simulation. To ensure that the numerical scheme satisfies the extended C-property we can define hydrostatic reconstruction as

$$h_{i+1/2}^- \coloneqq \max\{z_{b,i} + h_i - z^*, 0\}, \quad h_{i+1/2}^+ \coloneqq \max\{z_{b,i+1} + h_{i+1} - z^*, 0\}, \tag{7}$$

where $z^* \coloneqq \max\{z_{b,i}, z_{b,i+1}\}$, along with

$$(hu)_{i+1/2}^- \coloneqq u_i h_{i+1/2}^- \quad \text{and} \quad (hu)_{i+1/2}^+ \coloneqq u_{i+1} h_{i+1/2}^+. \tag{8}$$

Using this reconstruction we may show that

$$\tilde{G}_{i+1/2} \coloneqq \frac{1}{\Delta x}\left(\frac{1}{2} g (h_{i+1/2}^+)^2 - \frac{1}{2} g (h_{i+1/2}^-)^2\right)$$

is a first-order approximation of $gh\partial_x(h + z_b)$; indeed,

$$\begin{aligned} \tilde{G}_{i+1/2} &= \frac{g}{2\Delta x}(h_{i+1/2}^+ + h_{i+1/2}^-)(h_{i+1/2}^+ - h_{i+1/2}^-) \\ &= \frac{g}{2\Delta x}(h_i + h_{i+1} + \mathcal{O}(\Delta x))(\partial_x(h + z_b) + \mathcal{O}(\Delta x)), \end{aligned} \tag{9}$$

hence this last discretization is consistent with the system and independent of the bottom function.

Furthermore, by using the reconstruction (7), (8) we can see how the problem of Figure 2 is now solved. For that case, $z^* = \max\{z_{b,i}, z_{b,i+1}\} = z_{b,i+1}$, hence

$$h_{i+1/2}^- = \max\{z_{b,i} + h_i - z_{b,i+1}, 0\} = 0, \quad h_{i+1/2}^+ = \max\{z_{b,i+1} + h_{i+1} - z_{b,i+1}, 0\} = 0,$$

and therefore $\tilde{G}_{i+1/2} = 0$, which demonstrates that the extended C-property is satisfied.

Finally, as stated before, by using this reconstruction we may treat the system (4) as the (shallow water) system of conservation laws

$$\partial_t h + \partial_x(hu) = 0, \quad \partial_t(hu) + \partial_x\left(hu^2 + \frac{1}{2} g h^2\right) = 0.$$

In absence of an explicit bottom term the scheme (2), (3) now simplifies to (2) along with

$$\boldsymbol{D}^{\nu,\pm}_{i+1/2} = \frac{1}{2}(\boldsymbol{F}(\boldsymbol{W}^{\nu}_{i+1}) - \boldsymbol{F}(\boldsymbol{W}^{\nu}_{i}) \pm \boldsymbol{Q}^{\nu}_{i+1/2}(\boldsymbol{W}^{\nu}_{i+1} - \boldsymbol{W}^{\nu}_{i})).$$

2.5. **Linearized discontinuous non-hydrostatic model (**LDNH_0 **model)**

The LDNH_0 model of computational fluid dynamics (CFD) accounts for non-hydrostatic forces. In the present model a vertically constant profile for the horizontal velocity u and the vertical velocity w are assumed along with a linear vertical profile for the non-hydrostatic pressure p. This model is given by

$$\partial_t h + \partial_x(hu) = 0, \tag{10a}$$

$$\partial_t(hu) + \partial_x\left(hu^2 + \frac{1}{2}gh^2 + hp\right) = -(gh + 2p)z'_{\mathrm{b}}, \tag{10b}$$

$$\partial_t(hw) + \partial_x(huw) = 2p, \tag{10c}$$

$$\partial_x u + 2\frac{w - uz'_{\mathrm{b}}}{h} = 0. \tag{10d}$$

Since no evolution equation exists for p, this system is solved numerically by a projection method consisting of two steps per time step of length Δt.

(1) In the first step we solve the system

$$\begin{aligned} \partial_t h + \partial_x(hu) &= 0, \\ \partial_t(hu) + \partial_x\left(hu^2 + \frac{1}{2}gh^2\right) &= -(gh)z'_{\mathrm{b}}, \\ \partial_t(hw) + \partial_x(huw) &= 0, \end{aligned} \tag{11}$$

without the non-hydrostatic pressure. The homogeneous version of system (11) can be written as a first-order system

$$\partial_t \boldsymbol{W} + \partial_x \boldsymbol{F}(\boldsymbol{W}) = \boldsymbol{0}, \quad \boldsymbol{W} = (h, hu, hw)^{\mathrm{T}}, \quad \boldsymbol{F}(\boldsymbol{W}) = (hu, hu^2 + \frac{1}{2}gh^2, huw)^{\mathrm{T}},$$

where the eigenvalues of the flux Jacobian matrix $\partial \boldsymbol{F}(\boldsymbol{W})/\partial \boldsymbol{W}$ are given by

$$\lambda_1 = u - \sqrt{gh}, \quad \lambda_2 = u, \quad \lambda_3 = u + \sqrt{gh}, \tag{12}$$

and which is therefore hyperbolic. The system (11) has the form (1), so we can apply the aforementioned discretization and the hydrostatic reconstruction. The intermediate updated variables are given by

$$\boldsymbol{W}_i^{\nu+1/2} = \boldsymbol{W}_i^{\nu} - \frac{\Delta t}{\Delta x}(\boldsymbol{D}^{\nu,+}_{i-1/2} + \boldsymbol{D}^{\nu,-}_{i+1/2}).$$

In particular, since we are using an HLL viscosity matrix we can rewrite $\boldsymbol{D}^{\nu,\pm}_{i+1/2}$ as

$$\boldsymbol{D}^{\nu,\pm}_{i+1/2} = \frac{1}{2}((1 \pm \alpha_1)(\boldsymbol{F}(\boldsymbol{W}^{\nu}_{i+1}) - \boldsymbol{F}(\boldsymbol{W}^{\nu}_{i})) \pm \alpha_0(\boldsymbol{W}^{\nu}_{i+1} - \boldsymbol{W}^{\nu}_{i})). \tag{13}$$

(2) Once the first step is calculated, we can proceed with the second step, namely the projection step. In semi-discrete form this step can be written as

$$\frac{1}{\Delta t}(\boldsymbol{W}^{\nu+1} - \boldsymbol{W}^{\nu+1/2}) + ((\nabla P)^{\nu+1})^{\mathrm{T}} = \boldsymbol{0}, \tag{14}$$

where we define

$$\nabla P \coloneqq (0, \partial_x(hp) + 2pz_{\mathrm{b}}', -2p) = (0, \widetilde{\nabla P}), \quad \widetilde{\nabla P} \coloneqq (\partial_x(hp) + 2pz_{\mathrm{b}}', -2p).$$

Next, we define

$$\boldsymbol{X} \coloneqq \begin{pmatrix} u \\ w \end{pmatrix}, \quad \text{such that} \quad \boldsymbol{W} = \begin{pmatrix} h \\ h\boldsymbol{X} \end{pmatrix}.$$

Now (14) can be written as

$$\frac{h^{\nu+1} - h^{\nu+1/2}}{\Delta t} = 0, \tag{15a}$$

$$\frac{1}{\Delta t}((h\boldsymbol{X})^{\nu+1} - (h\boldsymbol{X})^{\nu+1/2}) + (\widetilde{\nabla P}^{\nu+1})^{\mathrm{T}} = \boldsymbol{0}. \tag{15b}$$

From (15a) we get $h^{\nu+1} = h^{\nu+1/2}$, whereas to solve (15b) we should use the constraint (10d) evaluated at time $t_{\nu+1}$. Replacing $h^{\nu+1}$, $u^{\nu+1}$ and $w^{\nu+1}$ from (15) in (10d) yields an equation for $p^{\nu+1}$. To state it, for sake of simplicity, we rename the time index $\nu + 1/2$ by $*$. The result is

$$\begin{aligned} &2(hw)^* - (hu)^*(\partial_x h^* + 2z_{\mathrm{b}}') + h^*\partial_x(hu)^* + \Delta t(p^{\nu+1}(4 + 2z_{\mathrm{b}}'(\partial_x h^* + 2z_{\mathrm{b}}')) \\ &+ \partial_x(h^* p^{\nu+1})(\partial_x h^* + 2z_{\mathrm{b}}') - 2h^*\partial_x(z_{\mathrm{b}}' p^{\nu+1}) - h^*\partial_{xx}(h^* p^{\nu+1})) = 0. \end{aligned} \tag{16}$$

To solve (16) numerically, we discretize this equation in space to obtain a linear system

$$\boldsymbol{T}\boldsymbol{P} = \boldsymbol{P}_0 \tag{17}$$

for $p_i^{\nu+1}$, where

$$\boldsymbol{P} = (p_0^{\nu+1}, p_1^{\nu+1}, \ldots, p_N^{\nu+1})^{\mathrm{T}}$$

is the vector of unknowns,

$$\boldsymbol{P}_0 = (p_{0,0}, p_{0,1}, \ldots, p_{0,N})^{\mathrm{T}} \tag{18}$$

is the vector of right-hand sides defined by (16), that is

$$p_{0,i} = (2(hw)^* - (hu)^*(\partial_x h^* + 2z_{\mathrm{b}}') + h^*\partial_x(hu)^*)|_{x=x_i}, \quad i = 0, \ldots, N, \tag{19}$$

and $\boldsymbol{T} = (T_{i,j})_{0 \le i,j \le N}$ is a tridiagonal matrix whose entries are defined by

$$\begin{aligned} T_{i,i} &= 4 + 2(z_{\mathrm{b}}'(\partial_x h^* + 2z_{\mathrm{b}}'))|_{x=x_i} + 2\frac{(h_i^*)^2}{\Delta x^2}, \\ T_{i,i+1} &= (\partial_x h^* + 2z_{\mathrm{b}}')|_{x=x_i}\frac{h_{i+1}^*}{2\Delta x} - \frac{h_i^* z_{\mathrm{b}}'|_{x=x_{i+1}}}{\Delta x} - \frac{h_i^* h_{i+1}^*}{\Delta x^2}, \\ T_{i,i-1} &= -(\partial_x h^* + 2z_{\mathrm{b}}')|_{x=x_i}\frac{h_{i-1}^*}{2\Delta x} + \frac{h_i^* z_{\mathrm{b}}'|_{x=x_{i-1}}}{\Delta x} - \frac{h_i^* h_{i-1}^*}{\Delta x^2}, \end{aligned}$$

and $T_{i,j} = 0$ for $|i - j| > 1$. Once the system (17) is solved, the values of $\boldsymbol{X}^{\nu+1/2}$ are updated to give $\boldsymbol{X}^{\nu+1}$, and a new iteration is started. In [27] it is shown that the projection method preserves the order of the hyperbolic method for this type of models.

2.6. **Forest forces**

Iimura and Tanaka [19] model the interaction between a tsunami and a forest through various forces and conduct experiments to validate them. Such forces are is the bed resistance per unit area

$$\tau_{\mathrm{b}} \coloneqq gm^2 \frac{hu|hu|}{\theta^2 h^{7/3}},$$

where m is the Manning roughness coefficient and θ is the forest porosity given by

$$\theta \coloneqq 1 - \frac{n_{\mathrm{t}} \pi d^2}{4},$$

where n_{t} is the vegetation density (number of trees per unit of area) and d is the diameter of the trees; the drag force per unit area

$$f_{\mathrm{D}} \coloneqq \frac{C_{\mathrm{D}} d n_{\mathrm{t}}}{2} \frac{hu|hu|}{\theta^2 h},$$

where C_{D} is the drag coefficient; and the inertia force per unit area

$$f_{\mathrm{M}} \coloneqq C_{\mathrm{M}} n_{\mathrm{t}} h \frac{\pi d^2}{4\theta} \partial_t \left(\frac{hu}{h} \right),$$

where C_{M} is the mass coefficient.

The drag coefficient C_{D} is usually obtained by calibration and is a dimensionless coefficient related to the geometry of the object. If the fluid is a liquid, then C_{D} depends on the Reynolds number; if the fluid is a gas, then C_{D} depends on both the Reynolds number and the Mach number. In our case, the reference area is $A_{\mathrm{ref}} = hd$; in general, A_{ref} depends on the type of drag coefficient. For automobiles and many other objects, the reference area is the projected frontal area of the vehicle. This may not necessarily be the cross-sectional area of the vehicle, depending on where the cross-section is taken. For example, for a sphere $A = \pi r^2$.

Incorporating the forces and the effect of porosity outlined in Section 1.6 into the non-hydrostatic LDNH_0 model (10) we get the non-hydrostatic LDNH_0 model specified for forest forces in final form:

$$\partial_t h + \frac{1}{\theta} \partial_x (hu) = 0, \tag{20a}$$

$$\partial_t (hu) + \frac{1}{\theta} \partial_x (hu^2) + \theta \partial_x \left(\frac{gh^2}{2} + hp \right) = -\theta (gh + 2p) z_{\mathrm{b}}' - \theta \tau_{\mathrm{b}} - \theta f_{\mathrm{D}} - \theta f_{\mathrm{M}}, \tag{20b}$$

$$\partial_t (hw) + \frac{1}{\theta} \partial_x (huw) = 2p, \tag{20c}$$

$$\partial_x u + 2 \frac{w - u z_{\mathrm{b}}'}{h} = 0. \tag{20d}$$

3. Discretization of the LDNH_0 model with forest forces

3.1. **An unstable discretization**

As a first step toward the discretization of (20) we define the functions k_1 and k_2 and the constant k_3 by

$$k_1(h) \coloneqq \frac{gm^2}{\theta h^{7/3}}, \quad k_2(h) \coloneqq \frac{C_{\mathrm{D}} d n_{\mathrm{t}}}{2\theta h}, \quad \text{and} \quad k_3 \coloneqq C_{\mathrm{M}} n_{\mathrm{t}} \frac{\pi d^2}{4}.$$

Equation (20b) can then be written as

$$\begin{aligned}&\partial_t(hu) + \frac{1}{\theta}\partial_x(hu^2) + \theta\partial_x(\frac{gh^2}{2} + hp)\\ &= -\theta(gh + 2p)z_{\mathrm{b}}' - (k_1 + k_2)(hu)|hu| - k_3\left(\partial_t(hu) - \frac{hu\partial_t h}{h}\right).\end{aligned}$$

Renaming $q_u \coloneqq hu$ and $q_w \coloneqq hw$ and keeping in mind that (20d) plays the role of a constraint, we may write (20a), (20b) and (20c) as the new system

$$\boldsymbol{M}\partial_t\begin{pmatrix}h\\ q_u\\ q_w\end{pmatrix} + \frac{1}{\theta}\partial_x\begin{pmatrix}q_u\\ q_u^2/h\\ q_u q_w/h\end{pmatrix} + \theta g h\partial_x\begin{pmatrix}0\\ h + z_{\mathrm{b}}\\ 0\end{pmatrix} + \theta\partial_x\begin{pmatrix}0\\ hp\\ 0\end{pmatrix} = \begin{pmatrix}0\\ -(k_1 + k_2)q_u|q_u|\\ 2p\end{pmatrix},$$

where we define the matrix

$$\boldsymbol{M} \coloneqq \begin{bmatrix}1 & 0 & 0\\ -(q_u/h)k_3 & 1 + k_3 & 0\\ 0 & 0 & 1\end{bmatrix}.$$

Using the notation

$$\boldsymbol{\mathcal{L}} \coloneqq \begin{pmatrix}\mathcal{L}_u\\ \mathcal{L}_{q_u}\\ \mathcal{L}_{q_w}\end{pmatrix} \coloneqq \frac{1}{\theta}\partial_x\begin{pmatrix}q_u\\ q_u^2/h\\ q_u q_w/h\end{pmatrix} + \theta g h\partial_x\begin{pmatrix}0\\ h + z_{\mathrm{b}}\\ 0\end{pmatrix} \tag{21}$$

we may rewrite the system as

$$\partial_t\begin{pmatrix}h\\ q_u\\ q_w\end{pmatrix} + \boldsymbol{C}\boldsymbol{\mathcal{L}} + \boldsymbol{C}\theta\partial_x\begin{pmatrix}0\\ hp\\ 0\end{pmatrix} = \boldsymbol{C}\begin{pmatrix}0\\ -(k_1 + k_2)q_u|q_u|\\ 2p\end{pmatrix}, \tag{22}$$

where we define

$$\boldsymbol{C} \coloneqq \boldsymbol{M}^{-1} = \begin{bmatrix}1 & 0 & 0\\ q_u k_3/((1 + k_3)h) & 1/(1 + k_3) & 0\\ 0 & 0 & 1\end{bmatrix}.$$

Assume now that $\boldsymbol{\mathcal{L}_i^\nu}$, $\mathcal{L}_{u,i}^\nu$, $\mathcal{L}_{q_u,i}^\nu$ and $\mathcal{L}_{q_w,i}^\nu$ are discrete versions of $\boldsymbol{\mathcal{L}}$, $\mathcal{L}_u$, $\mathcal{L}_{q_u}$ and $\mathcal{L}_{q_w}$, respectively, associated with $x = x_i$ and $t = t_\nu$. Then a discretization of (22) can be formulated as follows, where the term $q_u|q_u|$ is discretized as $q_{u,i}^{\nu+1}|q_{u,i}^\nu|$ for stability reasons:

$$\begin{aligned}h_i^{\nu+1} &= h_i^\nu - \Delta t\mathcal{L}_{u,i}^\nu,\\ q_{u,i}^{\nu+1} &= (q_{u,i}^\nu - \frac{\Delta t q_{u,i}^\nu k_3}{h^\nu(1 + k_3)}\mathcal{L}_{u,i}^\nu - \frac{\Delta t}{1 + k_3}\mathcal{L}_{q_u,i}^\nu - \theta\Delta t\frac{(\partial_x(hp))_i^{\nu+1}}{1 + k_3})\Big/(1 + \frac{(k_{1,i}^\nu + k_{2,i}^\nu)|q_{u,i}^\nu|\Delta t}{1 + k_3}),\\ q_{w,i}^{\nu+1} &= q_{w,i}^\nu - \Delta t\mathcal{L}_{q_w,i}^\nu + \Delta t 2p_i^{\nu+1}\end{aligned} \tag{23}$$

along with the constraint (20d). Notice that here we do not discretize the non-hydrostatic pressure terms because these are handled by the projection method.

The discrete version of (21) is chosen as

$$\boldsymbol{\mathcal{L}}_i^\nu = \frac{1}{\theta_i}(\boldsymbol{D}_{i-1/2}^{\nu,+} + \boldsymbol{D}_{i+1/2}^{\nu,-}),$$

where $\boldsymbol{D}^{\nu,\pm}_{i+1/2}$ is given by (13) and

$$\boldsymbol{F}(\boldsymbol{W}) = (q_u, \frac{q_u^2}{h} + \frac{gh^2}{2}, \frac{q_u q_w}{h})^{\mathrm{T}}.$$

Keep in mind that we are using a hydrostatic reconstruction, so, as is shown in (9), the term $gh\partial_x(h + z_b)$ can be computed in a conservative form as $\tilde{G}_{i+1/2}$. Thus, the first step is given by

$$\boldsymbol{W}_i^{\nu+1/2} = \boldsymbol{W}_i^{\nu} - \boldsymbol{C}_i^{-1}\frac{\Delta t}{\Delta x}(\boldsymbol{D}^{\nu,+}_{i-1/2} + \boldsymbol{D}^{\nu,-}_{i+1/2}).$$

This way to discretize the model turned out to be unstable due to the nature of the inertia force, so we should also evaluate $\boldsymbol{C}$ in the control volumes.

3.2. **A stable discretization**

An alternative discretization of the system (20) is based on applying the matrix $\boldsymbol{M}^{-1}$ within the discretization. To formulate it, we multiply the model

$$\boldsymbol{M}\partial_t \boldsymbol{W} + \partial_x \boldsymbol{F}(\boldsymbol{W}) + \boldsymbol{B}(\boldsymbol{W})\partial_x \boldsymbol{W} = \sigma' \boldsymbol{S}(\boldsymbol{W}) \tag{24}$$

by $\boldsymbol{M}^{-1}$ before space discretization. In (20), the term $\partial_x \boldsymbol{F}$ is multiplied by $1/\theta$, but to keep the method simple, we now assume that $1/\theta$ is part of $\boldsymbol{C}$, so in this subsection we utilize

$$\boldsymbol{C} \coloneqq \frac{1}{\theta}\boldsymbol{M}^{-1}, \tag{25}$$

hence pressure terms should be amplified by θ. Consequently, the system (24) is now written as

$$\partial_t \boldsymbol{W} + \boldsymbol{C}\partial_x \boldsymbol{F}(\boldsymbol{W}) + \boldsymbol{C}\boldsymbol{B}(\boldsymbol{W})\partial_x \boldsymbol{W} = \sigma'(x)\boldsymbol{C}\boldsymbol{S},$$

and can be discretized as

$$\boldsymbol{W}_i^{\nu+1} = \boldsymbol{N}_i(\boldsymbol{W}_i^{\nu} - \frac{\Delta t}{\Delta x}(\boldsymbol{D}^{\nu,+}_{i-1/2} + \boldsymbol{D}^{\nu,-}_{i+1/2})),$$

where we define the diagonal matrix

$$\boldsymbol{N}_i \coloneqq \mathrm{diag}(1, 1 \Big/ \left(1 + \frac{(k^{\nu}_{1,i} + k^{\nu}_{2,i})|q^{\nu}_{u,i}|\Delta t}{1 + k_3}\right), 1) = \mathrm{diag}(1, \frac{1 + k_3}{1 + k_3 + (k^{\nu}_{1,i} + k^{\nu}_{2,i})|q^{\nu}_{u,i}|\Delta t}, 1) \tag{26}$$

and $\boldsymbol{D}^{\nu,\pm}_{i+1/2}$ is given by

$$\begin{aligned}\boldsymbol{D}^{\nu,\pm}_{i+1/2} &= \frac{1}{2}\boldsymbol{C}_{i+1/2}(\boldsymbol{F}(\boldsymbol{W}^{\nu}_{i+1}) - \boldsymbol{F}(\boldsymbol{W}^{\nu}_{i}) \pm \boldsymbol{Q}^{\nu}_{i+1/2}(\boldsymbol{W}^{\nu}_{i+1} - \boldsymbol{W}^{\nu}_{i})) \\ &= \frac{1}{2}\boldsymbol{C}_{i+1/2}((1 \pm \alpha_1)(\boldsymbol{F}(\boldsymbol{W}^{\nu,+}_{i+1/2}) - \boldsymbol{F}(\boldsymbol{W}^{\nu,-}_{i+1/2})) \pm \alpha_0(\boldsymbol{W}^{\nu,+}_{i+1/2} - \boldsymbol{W}^{\nu,-}_{i+1/2})).\end{aligned}$$

Again, for sake of simplicity we do not consider non-hydrostatic pressure terms in these calculations, because we will use a projection method. However, these terms are easy to incorporate and their contribution must be equal to how it appears in (23).

This discretization of the system (20) turned out to be stable and will be applied in the remainder of this work.

3.3. **Eigenvalues**

Since external forces are taken into account, the eigenvalues will be different from the typical values $\lambda_0 = u$ and $\lambda_\pm = u \pm \sqrt{gh}$ (see (12)). In fact, our treatment requires calculating the eigenvalues of $\boldsymbol{CA}$, where $\boldsymbol{A} = \partial \boldsymbol{F}/\partial \boldsymbol{W}$ is the matrix of the system and $\boldsymbol{C}$ is given by (25), i.e.,

$$\begin{aligned}\boldsymbol{CA} &= \frac{1}{\theta}\begin{bmatrix} 1 & 0 & 0 \\ q_u k_3/((1+k_3)h) & 1/(1+k_3) & 0 \\ 0 & 0 & 1 \end{bmatrix}\begin{bmatrix} 0 & 1 & 0 \\ -q_u^2/h^2 + gh\theta^2 & 2q_u/h & 0 \\ -q_u q_w/h^2 & q_w/h & q_u/h \end{bmatrix} \\ &= \frac{1}{\theta}\begin{bmatrix} 0 & 1 & 0 \\ -q_u^2/((1+k_3)h^2) + gh\theta^2/(1+k_3) & (2+k_3)q_u/((1+k_3)h) & 0 \\ -q_u q_w/h^2 & q_w/h & q_u/h \end{bmatrix}.\end{aligned}$$

The eigenvalues of $\boldsymbol{CA}$ are

$$\lambda_1 = \frac{(2+k_3)u - \sqrt{4gh\theta^2(1+k_3) + u^2 k_3}}{2\theta(1+k_3)}, \quad \lambda_2 = \frac{u}{\theta}, \quad \lambda_3 = \frac{(2+k_3)u + \sqrt{4gh\theta^2(1+k_3) + u^2 k_3}}{2\theta(1+k_3)}.$$

3.4. **Scheme for the elliptic problem**

Once the hyperbolic step has been solved, one needs to correct the intermediate values (indexed by $\nu + 1/2$) and update the pressure value by solving an elliptic problem. As before we rename $()^{\nu+1/2}$ as $()^*$.

$$h^{\nu+1} = h^*, \tag{27a}$$

$$(hu)^{\nu+1} = (hu)^* - \Delta t\theta \frac{2p^{\nu+1} z_\mathrm{b}' + \partial_x (hp)^{\nu+1}}{1 + k_3 + (k_1^* + k_2^*)|h^* u^*|\Delta t}, \tag{27b}$$

$$(hw)^{\nu+1} = (hw)^* + 2\Delta t p^{\nu+1}, \tag{27c}$$

$$0 = 2(hw)^{\nu+1} - (hu)^{\nu+1}(\partial_x h^{\nu+1} + 2z_\mathrm{b}') + h^{\nu+1}\partial_x (hu)^{\nu+1}. \tag{27d}$$

Now, replacing (27a), (27b) and (27c) in (27d) yields

$$\begin{aligned}&2(hw)^* - (hu)^*(\partial_x h^* + 2z_\mathrm{b}') + h^*\partial_x (hu)^* + \Delta t(p^{\nu+1}(4 + 2z_\mathrm{b}'(\partial_x h^* + 2z_\mathrm{b}')f^*) \\ &+ \partial_x (h^* p^{\nu+1})(f^*(\partial_x h^* + 2z_\mathrm{b}') - h^*\partial_x (f^*)) - 2h^*\partial_x (f^* z_\mathrm{b}' p^{\nu+1}) - h^* f^* \partial_{xx}(h^* p^{\nu+1})) = 0,\end{aligned} \tag{28}$$

where we define

$$f \coloneqq \frac{\theta}{1 + k_3 + (k_1 + k_2)|hu|\Delta t}.$$

As we stated before, the elliptic equation (28) can be solved numerically writing the problem in the form $\boldsymbol{AP} = \boldsymbol{P}_0$, where $\boldsymbol{P}_0$ is given by (18), (19), $\boldsymbol{P}$ is the vector of unknowns and $\boldsymbol{A} = (A_{i,j})$ this time is a tridiagonal matrix given by

$$\begin{aligned}A_{i,i} &= 4 + 2(z_\mathrm{b}'(\partial_x h^* + 2z_\mathrm{b}')f)_i + 2\frac{(h_i^*)^2 f_i^*}{\Delta x^2}, \\ A_{i,i+1} &= (f^*(\partial_x h^* + 2z_\mathrm{b}') - h^*\partial_x f^*)_i \frac{h_{i+1}^*}{2\Delta_x} - \frac{h_i^*(f^* z_\mathrm{b}')_{i+1}}{\Delta x} - \frac{h_i^* h_{i+1}^* f_i^*}{\Delta x^2}, \\ A_{i,i-1} &= -(f^*(\partial_x h^* + 2z_\mathrm{b}') - h^*\partial_x f^*)_i \frac{h_{i-1}^*}{2\Delta_x} + \frac{h_i^*(f^* z_\mathrm{b}')_{i-1}}{\Delta x} - \frac{h_i^* h_{i-1}^* f_i^*}{\Delta x^2},\end{aligned}$$

and $A_{i,j} = 0$ for $|i - j| > 1$. Inverting this matrix we can find $\boldsymbol{P} = \boldsymbol{A}^{-1}\boldsymbol{P}_0$. Then we can correct the values of u and w.

4. LDNH$_0$ MULTILAYER MODEL

4.1. **Definition of multiple layers**

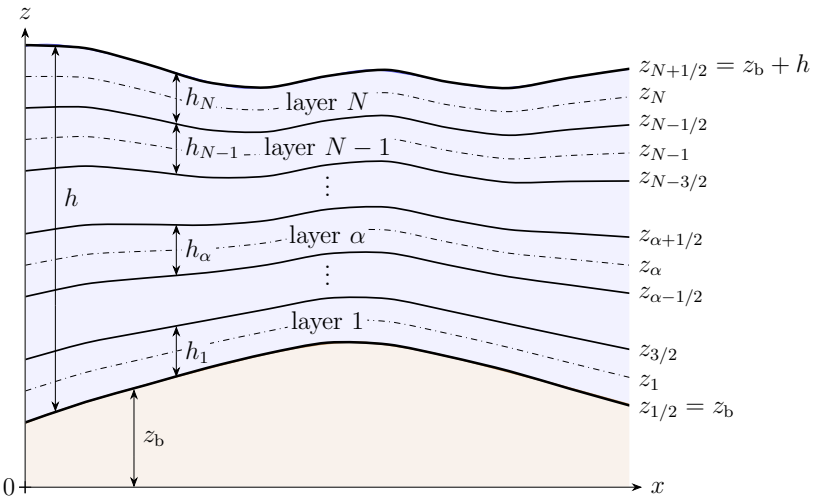

FIGURE 3. Definition of layers 1 to N, their interfaces (solid curves), and centerlines (dash-dotted).

According to standard definitions in the multilayer approach we subdivide the vertical interval between $z_{\mathrm{b}}(x)$ and $z_{\mathrm{b}}(x) + h(x,t)$ into N layers, layers 1 to N, of thickness $h_\alpha(x,t)$, $\alpha = 1, \ldots, N$, such that $h_1(x,t) + \cdots + h_N(x,t) = h(x,t)$ or equivalently, $l_1 + \cdots + l_N = 1$, where $l_\alpha = h_\alpha/h$, see Figure 3. Moreover, we define the layer interfaces

$$z_{\alpha+1/2} \coloneqq z_{\alpha+1/2}(x,t) \coloneqq z_{\mathrm{b}} + \sum_{\beta=0}^{\alpha} l_\beta h, \quad \alpha = 0, \ldots, N,$$

and the layer centerlines

$$z_\alpha \coloneqq z_\alpha(x,t) \coloneqq z_{\mathrm{b}} + \sum_{\beta=0}^{\alpha-1} l_\beta h + l_\alpha \frac{h}{2}, \quad \alpha = 1, \ldots, N.$$

where $z_{1/2} = z_{\mathrm{b}}$ is the bottom. This means that $z_{\alpha+1/2} - z_{\alpha-1/2} = l_\alpha h = h_\alpha$.

4.2. LDNH$_0$ **multilayer model (without forces and porosity)**

The shallow water equations are derived from a vertical integration of the Euler equations for an ideal fluid. In the same way, in the derivation of the LDNH$_0$ model we can subdivide vertical integration into multiple parts, each one with its own velocity, pressure, and size (layer thickness). The balance equations in differential

form for N layers resulting from the previous discussion are

$$\begin{aligned}
&\partial_t h + \partial_x(h\bar{\bar{u}}) = 0 \quad \text{with} \quad \bar{\bar{u}} = l_1\bar{u}_1 + \cdots + l_N\bar{u}_N,\\
&\partial_t(h_\alpha\bar{u}_\alpha) + \partial_x(h_\alpha\bar{u}_\alpha^2 + h_\alpha q_\alpha) - \partial_x z_{\alpha+1/2}q_{\alpha+1/2} + \partial_x z_{\alpha-1/2}q_{\alpha-1/2}\\
&= -gh_\alpha\partial_x\eta + \tilde{u}_{\alpha+1/2}\Gamma_{\alpha+1/2} - \tilde{u}_{\alpha-1/2}\Gamma_{\alpha-1/2},\\
&\partial_t(h_\alpha\bar{w}_\alpha) + \partial_x(h_\alpha\bar{u}_\alpha\bar{w}_\alpha) + q_{\alpha+1/2} - q_{\alpha-1/2}\\
&= \tilde{w}_{\alpha+1/2}\Gamma_{\alpha+1/2} - \tilde{w}_{\alpha-1/2}\Gamma_{\alpha-1/2}, \quad \alpha = 1,\ldots,N,
\end{aligned}$$

with $q_\alpha = \frac{1}{2}(q_{\alpha+1/2} + q_{\alpha-1/2})$ along with the diagnostic equations

$$\begin{aligned}
\bar{w}_\alpha - \bar{w}_{\alpha-1} - (\bar{u}_\alpha - \bar{u}_{\alpha-1})\partial_x z_{\alpha-1/2} - \frac{1}{2}(h_{\alpha-1}\partial_x\bar{u}_{\alpha-1} + h_\alpha\partial_x\bar{u}_\alpha) = 0, \quad \alpha = 2,\ldots,N,\\
\bar{w}_1 - \bar{u}_1\partial_x z_\mathrm{b} - \frac{1}{2}h_1\partial_x\bar{u}_1 = 0
\end{aligned}$$

and the boundary condition $q_{N+1/2} = 0$. (Here we recall that especially in the geophysical and meteorological context, a diagnostic equation is one that links the values of its variables simultaneously, either because the equation (or model) is time-independent, or the variables all refer to the values at the same time.)

The mass transfer term is given by

$$\Gamma_{\alpha+1/2} = \sum_{\beta=1}^{\alpha}\partial_x(h_\beta(\bar{u}_\beta - \bar{\bar{u}})).$$

Moreover, we define

$$\begin{aligned}
\tilde{u}_{\alpha+1/2} &\coloneqq (1-\gamma_{\alpha+1/2})\bar{u}_{\alpha+1} + \gamma_{\alpha+1/2}\bar{u}_\alpha,\\
\tilde{w}_{\alpha+1/2} &\coloneqq (1-\gamma_{\alpha+1/2})(\bar{w}_{\alpha+1} + \frac{h_{\alpha+1}}{2}\partial_x\bar{u}_{\alpha+1}) + \gamma_{\alpha+1/2}(\bar{w}_\alpha - \frac{h_\alpha}{2}\partial_x\bar{u}_\alpha)
\end{aligned}$$

for any $\gamma_{\alpha+1/2} \in [0,1]$. For sake of simplicity from we now rename $\bar{u}_\alpha$ as u_α and $\bar{w}_\alpha$ as w_α.

4.3. **Effect of porosity**

The porosity θ is a parameter related to the fraction of area available to be occupied by the fluid. In our case, since the vegetation uses a physical area, some regions cannot by fully filled by fluid. To determine how porosity affects the mass conservation equation we consider an infinitesimal element of area of the spatial domain $\Delta x\Delta h$ in a region with vegetation. In the x-direction we have an effective length $\theta_x\Delta x$ and in the z-direction an effective height $\theta_z\Delta h$. Then, if fluid with velocity u enters the area during a time interval of length Δt time, the balance equation becomes

$$\theta_x\theta_z\Delta x\Delta h = (hu(x_0) - hu(x_0+\theta_x\Delta x))\Delta t \approx -\theta_x\partial_x(hu)\Delta x\Delta t.$$

Simplifying, renaming θ_z as θ and taking the limit we obtain

$$\theta\partial_t h + \partial_x(hu) = 0.$$

4.4. **Transfer terms**

We now derive a formula for the transfer terms between layers. Let us consider the balance equation for layer α, namely

$$\theta_\alpha \partial_t h_\alpha + \partial_x(h_\alpha u_\alpha) = \frac{1}{l_\alpha}(\Gamma_{\alpha+1/2} - \Gamma_{\alpha-1/2}), \quad \alpha = 1, \dots, N.$$

Now, consider for a fixed $\alpha \in \{1, \dots, N\}$ the sums of the these equations from layer $\beta = 1$ to layer $\beta = \alpha$ and from layer $\beta = \alpha + 1$ to the last layer $\beta = N$. This yields

$$\begin{aligned}
\sum_{\beta=1}^{\alpha} l_\beta \theta_\beta \partial_t h_\beta + \sum_{\beta=1}^{\alpha} l_\beta \partial_x(h_\beta u_\beta) &= \Gamma_{\alpha+1/2} - \Gamma_{1/2}, \\
\sum_{\beta=\alpha+1}^{N} l_\beta \theta_\beta \partial_t h_\beta + \sum_{\beta=\alpha+1}^{N} l_\beta \partial_x(h_\beta u_\beta) &= \Gamma_{N+1/2} - \Gamma_{\alpha+1/2}.
\end{aligned}$$

Assuming that all layers have the same height at a given x-position, that is setting $h_\beta = h/N$ for all β, we obtain

$$(\partial_t h) \sum_{\beta=1}^{\alpha} \frac{\theta_\beta}{N} + \sum_{\beta=1}^{\alpha} \partial_x(h_\beta u_\beta) = \Gamma_{\alpha+1/2} - \Gamma_{1/2}, \tag{29}$$

$$(\partial_t h) \sum_{\beta=\alpha+1}^{N} \frac{\theta_\beta}{N} + \sum_{\beta=\alpha+1}^{N} \partial_x(h_\beta u_\beta) = \Gamma_{N+1/2} - \Gamma_{\alpha+1/2} \tag{30}$$

along with the equivalence

$$\bar{\theta} = \frac{1}{h} \int_{z_{1/2}}^{z_{N+1/2}} \theta(z) dz = \frac{1}{h} \sum_{\beta=1}^{N} \int_{z_{\beta-1/2}}^{z_{\beta+1/2}} \theta(z)\, \mathrm{d}z = \sum_{\beta=1}^{N} \frac{\theta_\beta}{N}.$$

Then we can rewrite equation (30) as

$$(\partial_t h) \left(\bar{\theta} - \sum_{\beta=1}^{\alpha} \frac{\theta_\beta}{N} \right) + \sum_{\beta=\alpha+1}^{N} \partial_x(h_\beta u_\beta) = \Gamma_{N+1/2} - \Gamma_{\alpha+1/2}. \tag{31}$$

To find the transfer terms we multiply (29) by $\bar{\theta} - \sum_{\beta=1}^{\alpha} \theta_\beta/N$ and (31) by $\sum_{\beta=1}^{\alpha} \theta_\beta/N$. Subtracting the results we obtain

$$\begin{aligned}
&\left(\bar{\theta} - \sum_{\beta=1}^{\alpha} \frac{\theta_\beta}{N} \right) \sum_{\beta=1}^{\alpha} \partial_x(h_\beta u_\beta) - \left(\sum_{\beta=1}^{\alpha} \frac{\theta_\beta}{N} \right) \sum_{\beta=\alpha+1}^{N} \partial_x(h_\beta u_\beta) \\
&= \left(\bar{\theta} - \sum_{\beta=1}^{\alpha} \frac{\theta_\beta}{N} \right) (\Gamma_{\alpha+1/2} - \Gamma_{1/2}) - \left(\sum_{\beta=1}^{\alpha} \frac{\theta_\beta}{N} \right) (\Gamma_{N+1/2} - \Gamma_{\alpha+1/2}).
\end{aligned} \tag{32}$$

Since the boundary transfer terms are zero, i.e., $\Gamma_{1/2} = \Gamma_{N+1/2} = 0$, (32) reduces to

$$\bar{\theta} \sum_{\beta=1}^{\alpha} \partial_x (h_\beta u_\beta) - \left(\sum_{\beta=1}^{\alpha} \frac{\theta_\beta}{N} \right) \sum_{\beta=1}^{N} \partial_x (h_\beta u_\beta) = \bar{\theta} \Gamma_{\alpha+1/2}$$

or equivalently,

$$\Gamma_{\alpha+1/2} = \sum_{\beta=1}^{\alpha} \partial_x (h_\beta u_\beta) - \left(\sum_{\beta=1}^{\alpha} \frac{\theta_\beta}{\bar{\theta} N} \right) \sum_{\beta=1}^{N} \partial_x (h_\beta u_\beta).$$

Alternatively, this equation can be written as

$$\Gamma_{\alpha+1/2} = \sum_{\beta=1}^{N} \gamma_{\alpha,\beta} \partial_x (h_\beta u_\beta), \quad \text{where} \quad \gamma_{\alpha,\beta} \coloneqq \begin{cases} 1 - \displaystyle\sum_{k=1}^{\alpha} \frac{\theta_k}{N\bar{\theta}} & \text{for } \alpha \geq \beta, \\ -\displaystyle\sum_{k=1}^{\alpha} \frac{\theta_k}{N\bar{\theta}} & \text{for } \alpha < \beta. \end{cases}$$

4.5. **Drag and inertia forces for the multilayer system**

A widely used definition of the drag force is

$$f_{\mathrm{D}} = \frac{1}{2} \rho C_{\mathrm{D}} A_{\mathrm{v}} |u| u,$$

where A_{v} is the effective "vertical" side face area of the object and C_{D} is the drag coefficient. Furthermore, to describe properties of individual trees, we use the height coordinate ζ that is measured from the ground surface, identified here with z_{b}. For trees, Tanaka et al. [29] characterize C_{D} by

$$C_{\mathrm{D}} = C_{\mathrm{D,ref}} \overline{c_{\mathrm{tr}} c_{\mathrm{le}}},$$

where we denote by $\overline{c_{\mathrm{tr}} c_{\mathrm{le}}}$ the vertical average of the product of the coefficients $c_{\mathrm{tr}}(\zeta)$ and $c_{\mathrm{le}}(\zeta)$ that represent the effect of the trunk and leaves of the trees, respectively:

$$\overline{c_{\mathrm{tr}} c_{\mathrm{le}}} \coloneqq \frac{1}{h} \int_0^h c_{\mathrm{tr}}(\zeta) c_{\mathrm{le}}(\zeta) \, \mathrm{d}\zeta$$

and $A_{\mathrm{v}} = dh$. Within a multilayer system the averages must be calculated for each layer α ($\alpha = 1, \ldots, N$). This is done by defining

$$C_{\mathrm{D},\alpha} \coloneqq C_{\mathrm{D,ref}} (\overline{c_{\mathrm{tr}} c_{\mathrm{le}}})_\alpha, \quad \text{where} \quad (\overline{c_{\mathrm{tr}} c_{\mathrm{le}}})_\alpha \coloneqq \frac{1}{h_\alpha} \int_{z_{\alpha-1/2} - z_{\mathrm{b}}}^{z_{\alpha+1/2} - z_{\mathrm{b}}} c_{\mathrm{tr}}(\zeta) c_{\mathrm{le}}(\zeta) \, \mathrm{d}\zeta, \quad \alpha = 1, \ldots, N.$$

On the other hand, if the diameter of a tree at height ζ is $d(\zeta)$, then we employ

$$A_{\mathrm{v},\alpha} \coloneqq h_\alpha \bar{d}_\alpha, \quad \text{where} \quad \bar{d}_\alpha \coloneqq \frac{1}{h_\alpha} \int_{z_{\alpha-1/2} - z_{\mathrm{b}}}^{z_{\alpha+1/2} - z_{\mathrm{b}}} d(\zeta) \, \mathrm{d}\zeta, \quad \alpha = 1, \ldots, N. \tag{33}$$

If we assume that the trees are symmetric along the z-axis the layer-specific transversal area $A_{\mathrm{t},\alpha}$ of each tree is $A_{\mathrm{t},\alpha} \coloneqq \pi (\bar{d}_\alpha)^2 / 4$ for $\alpha = 1, \ldots, N$. Summarizing all ingredients, we obtain that the drag force for one tree

associated with layer α is given by

$$f_{\mathrm{t},\alpha} \coloneqq \frac{1}{2}\rho C_{\mathrm{D},\alpha} A_{\mathrm{v},\alpha} |u_\alpha| u_\alpha = \frac{1}{2}\rho C_{\mathrm{D,ref}} (\overline{c_{\mathrm{tr}} c_{\mathrm{le}}})_\alpha \bar{d}_\alpha |h_\alpha u_\alpha| u_\alpha, \quad \alpha = 1, \ldots, N.$$

On the other hand, Tanaka et al. [29] calculate the effective density n_{t} of the forest as

$$n_{\mathrm{t}} = \frac{dnc_{\mathrm{tr}} c_{\mathrm{le}}}{A_{\mathrm{F}}},$$

where A_{F} is the forest area and

$$n = \frac{\text{number of trees}}{\text{forest length in flow direction}}.$$

Consequently, the effective forest density $n_{\mathrm{t},\alpha}$ and the corresponding porosity θ_α for layer α are given by the respective expressions

$$n_{\mathrm{t},\alpha} = \frac{\bar{d}_\alpha n (\overline{c_{\mathrm{tr}} c_{\mathrm{le}}})_\alpha}{A_{\mathrm{F}}}, \quad \theta_\alpha = 1 - \frac{n_{\mathrm{t}\alpha} \pi \bar{d}_\alpha^2}{4}.$$

Combining all ingredients we obtain the total forest drag force associated with layer α

$$f_{\mathrm{D},\alpha} = \frac{n_{\mathrm{t},\alpha}}{\theta_\alpha^2} f_{\mathrm{t},\alpha} = \frac{1}{2}\frac{n_{\mathrm{t},\alpha}}{\theta_\alpha^2} \rho C_{\mathrm{D,ref}} (\overline{c_{\mathrm{tr}} c_{\mathrm{le}}})_\alpha \bar{d}_\alpha |h_\alpha u_\alpha| u_\alpha, \quad \alpha = 1, \ldots, N.$$

Finally, assuming radial symmetry of the trees along the z-axis we obtain the inertia force

$$f_{\mathrm{M},\alpha} = C_{\mathrm{M}} \frac{n_{\mathrm{t},\alpha}}{\theta_\alpha} h_\alpha \frac{\pi \bar{d}_\alpha^2}{4} \partial_t \left(\frac{h_\alpha u_\alpha}{h_\alpha} \right), \quad \alpha = 1, \ldots, N.$$

4.6. **Gauckler-Manning friction and viscosity**

Within the multilayer approach the friction force with respect to the ground τ_α is present in the bottom layer only ($\alpha = 1$). Therefore, we define

$$\tau_\alpha \coloneqq k_{1,\alpha} |h_\alpha u_\alpha| h_\alpha u_\alpha = \begin{cases} \dfrac{gm^2 |u_\alpha| u_\alpha}{\theta_\alpha h^{1/3}} & \text{for } \alpha = 1, \\ 0 & \text{for } \alpha = 2, \ldots, N. \end{cases}$$

The upper layers will be not affected directly by this force, but physically, the interaction with the ground is transferred to the upper layers by the viscosity of the fluid. This phenomenon is modeled by additional viscosity terms $K_{\alpha+1/2}$ and $K_{\alpha-1/2}$ defined by

$$K_{\alpha+1/2} \coloneqq -\eta_0 \frac{u_{\alpha+1} - u_\alpha}{h_{\alpha+1} + h_\alpha}, \tag{34}$$

where we take into account that $K_{N+1/2} = 0$ and $K_{1/2} = -\tau_1$ and η_0 is the viscosity constant of the fluid. These viscosity therms are a simplified expression of the general case when each layer can have different size and fluids, see [15] for further explanations.

4.7. **Forces in the model**

Now, combining all the forces with the multilayer model, we arrive at the following governing equations of the multilayer approach:

$$\begin{aligned}
&\partial_t h_\alpha + \frac{\partial_x(h_\alpha u_\alpha)}{\theta_\alpha} - \frac{\Gamma_{\alpha+1/2}}{\theta_\alpha} + \frac{\Gamma_{\alpha-1/2}}{\theta_\alpha} = 0,\\
&\partial_t(h_\alpha u_\alpha) + \frac{\partial_x(h_\alpha u_\alpha^2)}{\theta_\alpha} + \theta_\alpha \partial_x(h_\alpha q_\alpha) - \theta_\alpha \partial_x z_{\alpha+1/2} q_{\alpha+1/2} + \theta_\alpha \partial_x z_{\alpha-1/2} q_{\alpha-1/2}\\
&= -g h_\alpha \theta_\alpha \partial_x \eta + \frac{\tilde{u}_{\alpha+1/2}\Gamma_{\alpha+1/2}}{\theta_\alpha} - \frac{\tilde{u}_{\alpha-1/2}\Gamma_{\alpha-1/2}}{\theta_\alpha} - f_{\mathrm{D}\alpha} - f_{\mathrm{M}\alpha} + \frac{K_{\alpha-1/2}}{\theta_\alpha} - \frac{K_{\alpha+1/2}}{\theta_\alpha},\\
&\partial_t(h_\alpha w_\alpha) + \frac{\partial_x(h_\alpha u_\alpha w_\alpha)}{\theta_\alpha} + q_{\alpha+1/2} - q_{\alpha-1/2} = \frac{\tilde{w}_{\alpha+1/2}\Gamma_{\alpha+1/2}}{\theta_\alpha} - \frac{\tilde{w}_{\alpha-1/2}\Gamma_{\alpha-1/2}}{\theta_\alpha},
\end{aligned} \tag{35}$$

where $\alpha = 1, \ldots, N$. Based on our previous calculations we get that we obtain the same kind of system of equations as (20) but this time for each layer.

4.8. **Solving the first-order system**

Initially, our focus is on solving the first-order equations of the problem. Therefore, we assume that all pressures in (35) are zero during this stage of the analysis. The impact of viscosity will be incorporated in the final stages of the calculations and, hence, is disregarded in this section. Similarly to our previous approach, we derive the flow rate equation by incorporating the relevant external forces, which can be expressed as

$$\begin{aligned}
&\partial_t(h_\alpha u_\alpha) + \frac{\partial_x(h_\alpha u_\alpha^2)}{\theta_\alpha} - \frac{\tilde{u}_{\alpha+1/2}\Gamma_{\alpha+1/2}}{\theta_\alpha} + \frac{\tilde{u}_{\alpha-1/2}\Gamma_{\alpha-1/2}}{\theta_\alpha}\\
&= -g h_\alpha \theta_\alpha \partial_x \eta - k_{2,\alpha}(h_\alpha u_\alpha)|h_\alpha u_\alpha| - k_{3,\alpha}\left(\partial_t(h_\alpha u_\alpha) - \frac{h_\alpha u_\alpha \partial_t h_\alpha}{h_\alpha}\right),\\
&(1+k_{3,\alpha})\partial_t(h_\alpha u_\alpha) - k_{3,\alpha} u_\alpha \partial_t h_\alpha + \frac{\partial_x(h_\alpha u_\alpha^2)}{\theta_\alpha} - \frac{\tilde{u}_{\alpha+1/2}\Gamma_{\alpha+1/2}}{\theta_\alpha} + \frac{\tilde{u}_{\alpha-1/2}\Gamma_{\alpha-1/2}}{\theta_\alpha}\\
&= -g h_\alpha \theta_\alpha \partial_x \eta - k_{2,\alpha}(h_\alpha u_\alpha)|h_\alpha u_\alpha|,
\end{aligned}$$

where we define the constants

$$k_{2,\alpha} \coloneqq \frac{C_{\mathrm{D},\alpha} d_\alpha n_{\mathrm{t},\alpha}}{2\theta h_\alpha} \quad \text{and} \quad k_{3,\alpha} = C_{\mathrm{M}} \frac{n_{\mathrm{t},\alpha}\pi \bar{d}_\alpha^2}{4}.$$

For every $\alpha = 1, \ldots, N$ we need to solve the system of balance equations

$$\boldsymbol{\mathcal{M}}_\alpha \partial_t \begin{pmatrix} h_\alpha \\ h_\alpha u_\alpha \\ h_\alpha w_\alpha \end{pmatrix} + \frac{1}{\theta_\alpha}\partial_x \begin{pmatrix} h_\alpha u_\alpha \\ h_\alpha u_\alpha^2 \\ h_\alpha u_\alpha w_\alpha \end{pmatrix} + \frac{1}{\theta_\alpha}\begin{bmatrix} \boldsymbol{B}_{h,\alpha} \\ \boldsymbol{B}_{hu,\alpha} \\ \boldsymbol{B}_{hw,\alpha} \end{bmatrix} \partial_x \boldsymbol{W} = -\begin{pmatrix} 0 \\ k_{2,\alpha}(h_\alpha u_\alpha)|h_\alpha u_\alpha| \\ 0 \end{pmatrix}, \tag{36}$$

where we define

$$\boldsymbol{\mathcal{M}}_\alpha \coloneqq \begin{bmatrix} 1 & 0 & 0 \\ -u_\alpha k_{3,\alpha} & 1+k_{3,\alpha} & 0 \\ 0 & 0 & 1 \end{bmatrix}$$

and $\boldsymbol{B}_{h,\alpha}$, $\boldsymbol{B}_{hu,\alpha}$ and $\boldsymbol{B}_{hw,\alpha}$ represent the corresponding rows of $\boldsymbol{B}_\alpha$. Since the transfer terms depend on the velocities of all layers, $\boldsymbol{W}$ is a vector defined as

$$\boldsymbol{W} \coloneqq (h_1, h_1u_1, h_1w_1, h_2, h_2u_2, h_2w_2, \ldots, h_N, h_Nu_N, h_Nw_N)^{\mathrm{T}} \in \mathbb{R}^{3N}.$$

Multiplying (36) from the left by

$$\boldsymbol{\mathcal{C}}_\alpha \coloneqq \boldsymbol{\mathcal{M}}_\alpha^{-1} = \begin{bmatrix} 1 & 0 & 0 \\ u_\alpha k_{3,\alpha}/(1+k_{3,\alpha}) & 1/(1+k_{3,\alpha}) & 0 \\ 0 & 0 & 1 \end{bmatrix}$$

we obtain

$$\partial_t \begin{pmatrix} h_\alpha \\ h_\alpha u_\alpha \\ h_\alpha w_\alpha \end{pmatrix} + \frac{1}{\theta_\alpha}\mathcal{C}_\alpha \partial_x \begin{pmatrix} h_\alpha u_\alpha \\ h_\alpha u_\alpha^2 \\ h_\alpha u_\alpha w_\alpha \end{pmatrix} + \frac{1}{\theta_\alpha}\mathcal{C}_\alpha \begin{bmatrix} \boldsymbol{B}_{h,\alpha} \\ \boldsymbol{B}_{hu,\alpha} \\ \boldsymbol{B}_{hw,\alpha} \end{bmatrix} \partial_x \boldsymbol{W} = -\boldsymbol{\mathcal{C}}_\alpha \begin{pmatrix} 0 \\ k_{2,\alpha}(h_\alpha u_\alpha)|h_\alpha u_\alpha| \\ 0 \end{pmatrix}. \tag{37}$$

Now we can use the FV method described before to numerically solve the system of PDEs (37), but to improve the stability of the numerical scheme we discretize the remaining external forces in a semi-implicit form, this means that $h_\alpha u_\alpha|h_\alpha u_\alpha|$ is evaluated as

$$h_\alpha u_\alpha|h_\alpha u_\alpha| \approx (h_\alpha u_\alpha)^{\nu+1}|h_\alpha u_\alpha|^{\nu}.$$

Consequently, the hyperbolic scheme for layer α becomes

$$\boldsymbol{W}_{\alpha,i}^{\nu+1} = \boldsymbol{N}_{\alpha,i}(\boldsymbol{W}_{\alpha,i}^{\nu} - \frac{\Delta t}{\Delta x}(\boldsymbol{D}_{\alpha,i-1/2}^{\nu,+} + \boldsymbol{D}_{\alpha,i+1/2}^{\nu,-})),$$

where the diagonal matrix $\boldsymbol{N}_\alpha$ is defined analogously to (26); namely we here get

$$\boldsymbol{N}_{\alpha,i} \coloneqq \operatorname{diag}(1, 1 \Big/ (1 + \frac{k_{2,\alpha}^{\nu}|h_{\alpha,i}^{\nu}u_{\alpha,i}^{\nu}|\Delta t}{1+k_{3,\alpha}}), 1) = \operatorname{diag}(1, \frac{1+k_{3,\alpha}}{1+k_{3,\alpha}+k_{2,\alpha}^{\nu}|h_{\alpha,i}^{\nu}u_{\alpha,i}^{\nu}|\Delta t}, 1),$$

and

$$\begin{aligned}\boldsymbol{D}_{\alpha,i+1/2}^{\nu,\pm} = \frac{1}{2\theta_{\alpha,i+1/2}^{\nu}}\boldsymbol{\mathcal{C}}_{\alpha,i+1/2}^{\nu}(\boldsymbol{F}(\boldsymbol{W}_{\alpha,i+1}^{\nu}) - \boldsymbol{F}(\boldsymbol{W}_{\alpha,i}^{\nu}) + \boldsymbol{B}_{\alpha,i+1/2}^{\nu}(\boldsymbol{W}_{\alpha,i+1}^{\nu} - \boldsymbol{W}_{\alpha,i}^{\nu}) \\ \pm \boldsymbol{Q}_{\alpha,i+1/2}^{\nu}(\boldsymbol{W}_{\alpha,i+1}^{\nu} - \boldsymbol{W}_{\alpha,i}^{\nu})).\end{aligned}$$

4.9. **Projection matrix**

Similarly to (27) the elliptic problems for each layer can be written as

$$\begin{aligned} h^{\nu+1} &= h^* \\ (h_\alpha u_\alpha)^{\nu+1} &= (h_\alpha u_\alpha)^* + \Delta t f_\alpha^*(\partial_x z_{\alpha+1/2}^* q_{\alpha+1/2}^{\nu+1} - \partial_x z_{\alpha-1/2}^* q_{\alpha-1/2}^{\nu+1} - h_\alpha^* q_\alpha^{\nu+1}), \\ (h_\alpha w_\alpha)^{\nu+1} &= (h_\alpha w_\alpha)^* - \Delta t(q_{\alpha+1/2}^{\nu+1} - q_{\alpha-1/2}^{\nu+1}), \end{aligned} \tag{38}$$

where f_α represents the multiplicative factors caused by the treatment of the vegetation forces, i.e.,

$$f_\alpha = \frac{\theta_\alpha}{1 + k_{3,\alpha} + k_{2,\alpha}|h_\alpha u_\alpha|\Delta t}.$$

For $\alpha = 2, \ldots, N$ the constraints can be rewritten as

$$h_\alpha w_\alpha - h_\alpha w_{\alpha-1} - h_\alpha u_\alpha \partial_x z_\alpha + h_{\alpha-1} u_{\alpha-1} \partial_x z_{\alpha-1} + \frac{h_\alpha}{2} \partial_x \left(h_\alpha u_\alpha + h_{\alpha-1} u_{\alpha-1} \right) = 0 \tag{39}$$

and for the first layer ($\alpha = 1$) as

$$h_1 w_1 - h_1 u_1 \partial_x z_1 + \frac{h_1}{2} \partial_x (h_1 u_1) = 0 \tag{40}$$

Typically, the variables are evaluated in volumes while the pressures are defined on the edges. To apply the projection method, we discretize the terms $(h_\alpha u_\alpha)^{\nu+1}$ and $(h_\alpha w_\alpha)^{\nu+1}$ on the edges and substitute them into the constraint equations (39) and (40). Alternatively, we can substitute these terms into the constraint equations (39) and (40) first and then discretize them "at $i + 1/2$", that is, on the edges. In this context, we have opted for the latter approach, which yields the equation

$$\begin{aligned}
\frac{4N^2 P^*}{\Delta t} &+ q_{\alpha-1/2}(8N^2 + f_\alpha \phi_\alpha^2 + f_{\alpha-1}\phi_{\alpha-1}^2 - h\partial_x(f_\alpha \phi_\alpha) + h\partial_x(f_{\alpha-1}\phi_{\alpha-1})) \\
&-(\partial_x q_{\alpha-1/2})(h\partial_x(f_\alpha h) + h\partial_x(f_{\alpha-1}h)) - \partial_{xx} q_{\alpha-1/2}(h^2(f_\alpha + f_{\alpha-1})) \\
&+q_{\alpha-3/2}(2N^2 + f_{\alpha-1}\phi_{\alpha-1}^2 + h\partial_x(f_{\alpha-1}\phi_{\alpha-1})) \\
+(\partial_x q_{\alpha-3/2})(h f_{\alpha-1}\phi_{\alpha-1} &+ h^2 \partial_x(f_{\alpha-1}) + h f_{\alpha-1}\phi_{\alpha-1/2}) + (\partial_{xx} q_{\alpha-3/2})(h^2 f_{\alpha-1}) \\
&+q_{\alpha+1/2}(2N^2 + f_\alpha \phi_\alpha^2 - h\partial_x(f_\alpha \phi_\alpha)) \\
&+(\partial_x q_{\alpha+1/2})(h f_\alpha \phi_\alpha + h^2 \partial_x(f_\alpha) + h f_\alpha \phi_{\alpha-1/2}) + \partial_{xx} q_{\alpha+1/2}(h^2 f_\alpha) = 0,
\end{aligned} \tag{41}$$

where P^* are the independent terms. The system (41) is solved numerically by an iterative Jacobi method. In this way we only need to write out the part of the matrix associated with $q_{\alpha-1/2}$. If we denote this matrix by $\boldsymbol{M} = (M_{i,j})$ then

$$\begin{aligned}
M_{i,i} &= 8N^2 + f_\alpha \phi_\alpha^2 + f_{\alpha-1}\phi_{\alpha-1}^2 - h_{i+1/2}\partial_x(f_{\alpha,i+1/2}\phi_{\alpha,i+1/2}) + h_{i+1/2}\partial_x(f_{\alpha-1,i+1/2}\phi_{\alpha-1}) \\
&\quad + \frac{2}{\Delta x^2} h_{i+1/2}^2 (f_{\alpha,i+1/2} + f_{\alpha-1,i+1/2}), \\
M_{i,i+1} &= -\frac{1}{2\Delta x}(h_{i+1/2}\partial_x(f_{\alpha,i+1/2}h_{i+1/2}) + h_{i+1/2}\partial_x(f_{\alpha-1,i+1/2}h_{i+1/2})) \\
&\quad - \frac{1}{\Delta x^2} h_{i+1/2}^2 (f_{\alpha,i+1/2} + f_{\alpha-1,i+1/2}), \\
M_{i,i-1} &= \frac{1}{2\Delta x}(h_{i+1/2}\partial_x(f_{\alpha,i+1/2}h_{i+1/2}) + h_{i+1/2}\partial_x(f_{\alpha-1,i+1/2}h_{i+1/2})) \\
&\quad - \frac{1}{\Delta x^2} h_{i+1/2}^2 (f_{\alpha,i+1/2} + f_{\alpha-1,i+1/2})
\end{aligned}$$

and $M_{i,j} = 0$ for $|i - j| > 1$. Notice that $\partial_x h = \phi_\alpha - \phi_{\alpha-1}$, where

$$\phi_\alpha = 2N\partial_x \left(z_{\alpha-1/2} + \frac{h_\alpha}{2} \right).$$

As stated before, once the values of $q_{\alpha-3/2}$, $q_{\alpha-1/2}$ and $q_{\alpha+1/2}$ have been found for each layer, we must update the values of u_α and w_α for each layer using (38).

4.10. **Adding viscosity and friction**

At this point we have variables evaluated at time step $t_{\nu+1}$ but we must add the viscosity effect, so we will rename this time as $*$ and because we are only correcting the velocity, thereby omitting the superscript in h_α. Thus, we obtain

$$h_\alpha u_\alpha^{\nu+1} = h_\alpha u_\alpha^* + \frac{\Delta t}{\theta_\alpha} K_{\alpha-1/2}^{\nu+1} - \frac{\Delta t}{\theta_\alpha} K_{\alpha+1/2}^{\nu+1}.$$

By using the definition (34) we get

$$\begin{aligned}
h_1 u_1^{\nu+1} &= h_1 u_1^* - \Delta t k_1 |h_1 u_1^*| h_1 u_1^{\nu+1} + \Delta t \frac{\eta_0}{2\theta_\alpha} \frac{u_2^{\nu+1} - u_1^{\nu+1}}{h_1}, \\
h_\alpha u_\alpha^{\nu+1} &= h_\alpha u_\alpha^* - \Delta t \frac{\eta_0}{2\theta_\alpha} \frac{u_\alpha^{\nu+1} - u_{\alpha-1}^{\nu+1}}{h_\alpha} + \Delta t \frac{\eta_0}{2\theta_\alpha} \frac{u_{\alpha+1}^{\nu+1} - u_\alpha^{\nu+1}}{h_\alpha}, \quad \alpha = 2, \ldots, N-1, \\
h_N u_N^{\nu+1} &= h_N u_N^* - \Delta t \frac{\eta_0}{2\theta_\alpha} \frac{u_N^{\nu+1} - u_{N-1}^{\nu+1}}{h_N}.
\end{aligned}$$

For the unknowns $u_1^{\nu+1}, \ldots, u_N^{\nu+1}$ we obtain the system

$$\begin{aligned}
(1 + \frac{\eta_0 \Delta t}{2\theta_\alpha h_1^2} + \Delta t k_1 |h_1 u_1^*|) h_1 u_1^{\nu+1} - \frac{\eta_0 \Delta t}{2\theta_\alpha h_\alpha^2} h_\alpha u_2^{\nu+1} &= h_1 u_1^*, \\
(1 + \frac{\eta_0 \Delta t}{\theta_\alpha h_\alpha^2}) h_\alpha u_\alpha^{\nu+1} - \frac{\eta_0 \Delta t}{2\theta_\alpha h_\alpha^2} h_\alpha u_{\alpha-1}^{\nu+1} - \frac{\eta_0 \Delta t}{2\theta_\alpha h_\alpha^2} h_\alpha u_{\alpha+1}^{\nu+1} &= h_\alpha u_\alpha^*, \quad \alpha = 2, \ldots, N-1, \\
(1 + \frac{\eta_0 \Delta t}{2\theta_\alpha h_N^2}) h_N u_N^{\nu+1} - \frac{\eta_0 \Delta t}{2\theta_\alpha h_\alpha^2} h_\alpha u_{N-1}^{\nu+1} &= h_N u_N^*.
\end{aligned}$$

This linear system of equations can be written as a tridiagonal matrix and solved by a Thomas algorithm.

5. Numerical results

5.1. **Example 1: convergence test**

Table 1. Example 1: convergence test (comparison with an exact soliton solution).

Number of cells $\mathcal{J}$	L^1 error e_h	rate	L^1 error e_{hu}	rate	L^1 error e_{hw}	rate
50	1.17E-02	—	3.99E-02	—	1.14E-02	—
100	5.30E-03	1.14	1.78E-02	1.16	6.20E-03	0.88
200	3.00E-03	0.82	1.01E-02	0.82	3.80E-03	0.71
400	1.70E-03	0.82	5.70E-03	0.83	2.20E-03	0.79
800	9.11E-04	0.90	3.00E-03	0.93	1.20E-03	0.87
1600	4.75E-04	0.94	1.60E-03	0.91	6.56E-04	0.87

As a first test of the accuracy of the scheme we consider the exact soliton solution of the LDNH_0 soliton, which is described in Appendix A. The computational domain considered is the x-interval $X = [-25, 25]$, which is subdivided into $\mathcal{J}$ subintervals of length $\Delta x = 50/\mathcal{J}$, and we let $\varphi(x_i, t)$ denote the numerical approximation

of the exact value $\varphi_{\text{exact}}(x_i, t)$. We measure the L^1 error in φ at simulated time $t = 10\,\text{s}$ as follows:

$$e_\varphi(t) \coloneqq \frac{1}{N} \sum_{x_i \in X} |\varphi(x_i, t) - \varphi_{\text{exact}}(x_i, t)|;$$

this is done for $\varphi = h$, $\varphi = hu$ and $\varphi = hw$. We utilize a CFL number of 0.8 and obtain the errors displayed in Table 1. We observe that the error decreases at a rate slightly smaller than one, in agreement with the formal first-order accuracy of the numerical scheme.

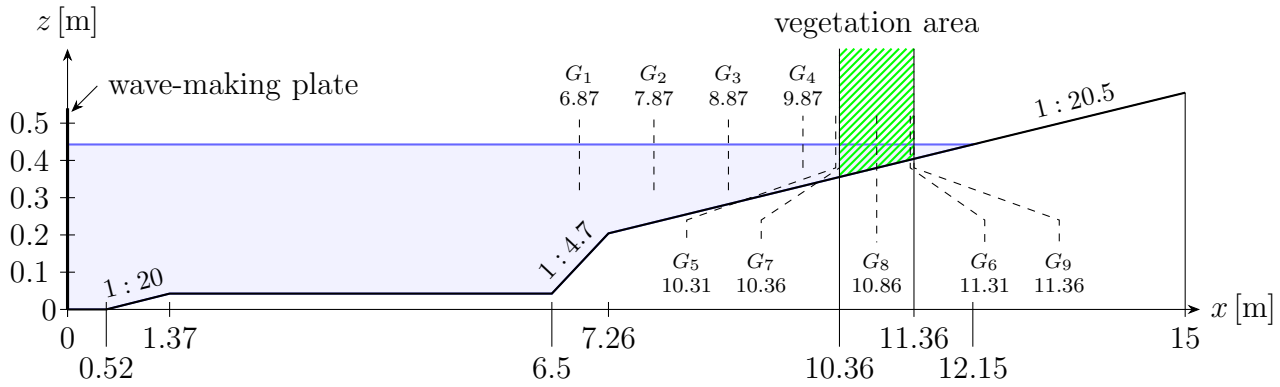

FIGURE 4. Schematic of the experiment, showing the positions of the nine measurement points $G_1, \ldots, G_9$. The positions of G_1 to G_6 are fixed, G_7 and G_8 are in front of and behind the vegetation, and G_8 is in the middle of the vegetation for uniform arrangements (in this study, Cases 1, 3 and 5 of [19]) and at the boundary of two different tree densities in the combined arrangements (in this work, Cases 8 and 13 of [19]). The specific situation in this plot with $G_7 = 10.36\,\text{m}$, $G_8 = 10.36\,\text{m}$ and $G_9 = 11.36\,\text{m}$ corresponds to Case 1. Notice that the vertical scale is five times larger than the horizontal.

5.2. **Examples 2 to 6: Iimura-Tanaka experiments and tests for the LDNH_0 single-layer model**

The model and numerical method are motivated by a series of experiments reported by Iimura and Tanaka [19] that represents a scale 1:100 scenario for a real-world tsunami. The experimental setup consists in a channel of width 0.4 m and length 15 m with a bottom topography representing a beach (coastal area) with two slopes, see [19, Figure 1] and our Figure 4. At the seaward end of the channel, at $x = 0\,\text{m}$, a wave-making plate is located, and between $x = 10.36\,\text{m}$ and $x = 11.36\,\text{m}$ various arrangements of vertical cylinders, each with a diameter of $d = 0.005\,\text{m}$ can be placed to model the coastal vegetation (see Figure 5). The level of water at rest is 0.4 m. The run-up height, water level, and force acting on a cylinder were measured at nine different points ($G_1, \ldots, G_9$; see Figure 4 for the corresponding x-positions).

Among the 15 different distributions of coastal vegetation tested in [19], Cases 1 to 15, we used five, namely Cases 1, 3, 5, 8, and 13, for numerical simulation. To specify the corresponding parameters, we recall from [19] that for given a tree distribution such as the one drawn in Figure 5, the thickness of vegetation is calculated as

$$d_n = \frac{2}{\sqrt{3} D_{\text{f}}^2} W_{\text{f}} d \times 10^5 + \frac{2}{\sqrt{3} D_{\text{b}}^2} W_{\text{b}} d \times 10^5, \tag{42}$$

where the factor 10^5 adjusts a unit of d_n because D and W are measured in millimeters and d in meters. In the experiments, d_n was set to a constant 231 in all experiments [19]. The width of the channel is 0.4 m; then,

the tree density, measures in trees per square metre, can be calculated as

$$n_{\mathrm{t}} = \frac{d_n}{W \times 0.4\,\mathrm{m}}. \tag{43}$$

The wave-making plate at $x = 0\,\mathrm{m}$ generates a solitary wave with a height of 3.14 cm in the vicinity of the left boundary.

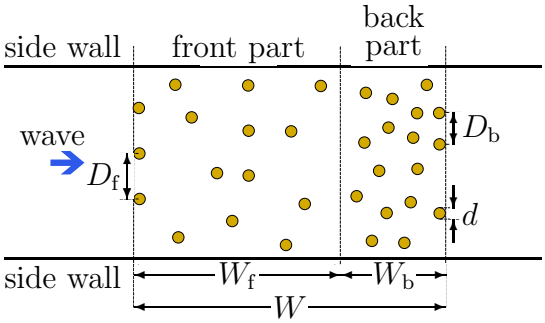

FIGURE 5. Schematic of the distribution of trees in the experiment, as seen from above.

TABLE 2. Parameters of Cases 1, 3, 5, 8, and 13 of Iimura and Tanaka [19]. The mass coefficient, the tree diameter, and the Manning roughness coefficient are $C_{\mathrm{M}} = 2$, $d = 5\,\mathrm{mm}$, and $m = 0.0108$, respectively, in all cases. The definition of $C_{\mathrm{D}} = C_{\mathrm{D}}(x)$ is provided in the text.

	Case 1	Case 3	Case 5	Case 8	Case 13
tree spacing, back part D_{b} [mm]	50	30	10	40	20
tree spacing, front part D_{f} [mm]	0	0	0	20	40
length of back part W_{b} [mm]	0	360	40	320	80
length of front part W_{f} [mm]	1000	0	0	80	320
position of start of forest x_{F} [m]	10.32	11.00	11.32	10.96	10.96

The parameters defining the five cases considered herein are given in Table 2. To describe the definitions of the drag coefficient C_{D} as a function of x, we denote in Cases 1, 3 and 5 by x_7, x_8 and x_9 the location of measurement points G_7, G_8, and G_9, respectively.

In Case 1, $C_{\mathrm{D}}(x)$ is a piecewise linear interpolation of $C_{\mathrm{D}}(x_7) = 0.71$, $C_{\mathrm{D}}(x_8) = 0.94$ and $C_{\mathrm{D}}(x_9) = 0.77$, corresponding to the variable drag coefficient at the beginning, the middle, and the end of the forest. Furthermore, in Case 1 we obtain from (43) (with $d_n = 231$ and $W = 1\,\mathrm{m}$) a tree density of $n_{\mathrm{t}} = 577.5\,\mathrm{m}^{-2}$. The experimental data corresponding to this case are plotted in Figure 6 (a). Analogously, in Case 3, $C_{\mathrm{D}}(x)$ is a piecewise linear interpolation of $C_{\mathrm{D}}(x_7) = 0.66$, $C_{\mathrm{D}}(x_8) = 0.79$ and $C_{\mathrm{D}}(x_9) = 0.94$. It is this scenario for which (42) produces $d_n = 231$, the value which is used throughout, and evaluating (43) we get for Case 3 $n_{\mathrm{t}} = 1604.1\bar{6}\,\mathrm{m}^{-2}$. The experimental data corresponding to Case 3 are plotted in Figure 6 (b). For Case 5, $C_{\mathrm{D}}(x)$ is a piecewise linear interpolation of $C_{\mathrm{D}}(x_7) = 1.73$, $C_{\mathrm{D}}(x_8) = 1.32$ and $C_{\mathrm{D}}(x_9) = 2.23$, and from (43) we now get $n_{\mathrm{t}} = 14437.5\,\mathrm{m}^{-2}$. The experimental data corresponding to Case 5 are plotted in Figure 6 (c).

Cases 1, 3, and 5 of [19] belong to the group of experiments (Cases 1 to 5 of [19]) where there is either no front part or no back part (see Table 2), that is the composition of the vegetation area is constant. In contrast, Cases 8 and 13 are part of the experiments (Cases 6 to 15 of [19]) with a change of the forest structure close to x_8. Consequently, the drag coefficient is a piecewise linear function interpolating four different values corresponding to $C_{\mathrm{D}}(x_7)$, $C_{\mathrm{D}}(x_{8,\mathrm{f}})$ which is the drag coefficient determined by the "front part" (the forest immediately to the

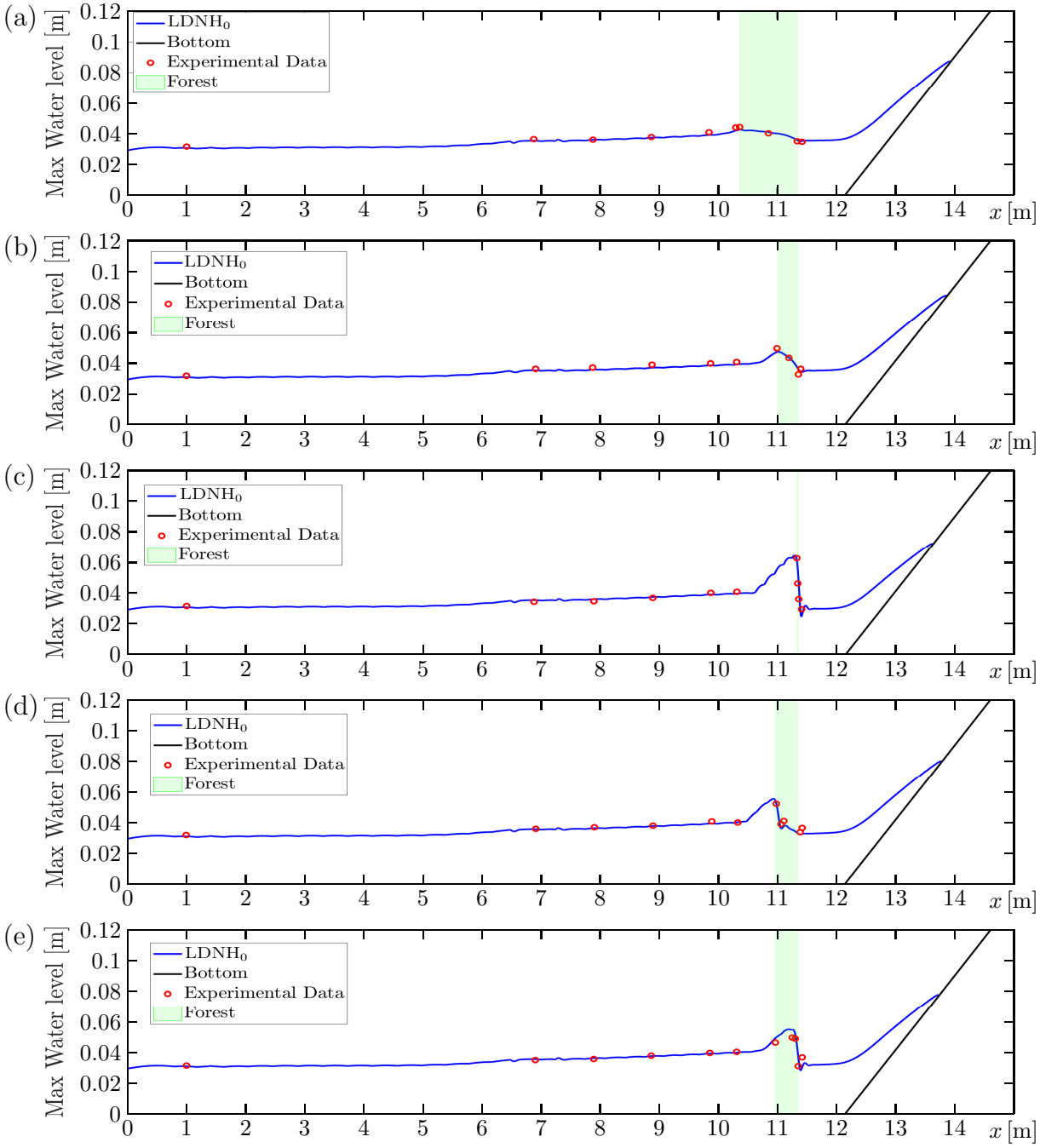

FIGURE 6. Examples 2 to 6: experimental data (red dots) and LDNH$_0$ simulations for (a) Example 2 [19, Case 1], (b) Example 3 [19, Case 3], (c) Example 4 [19, Case 5], (d) Example 5 [19, Case 8] and (e) Example 6 [19, Case 13].

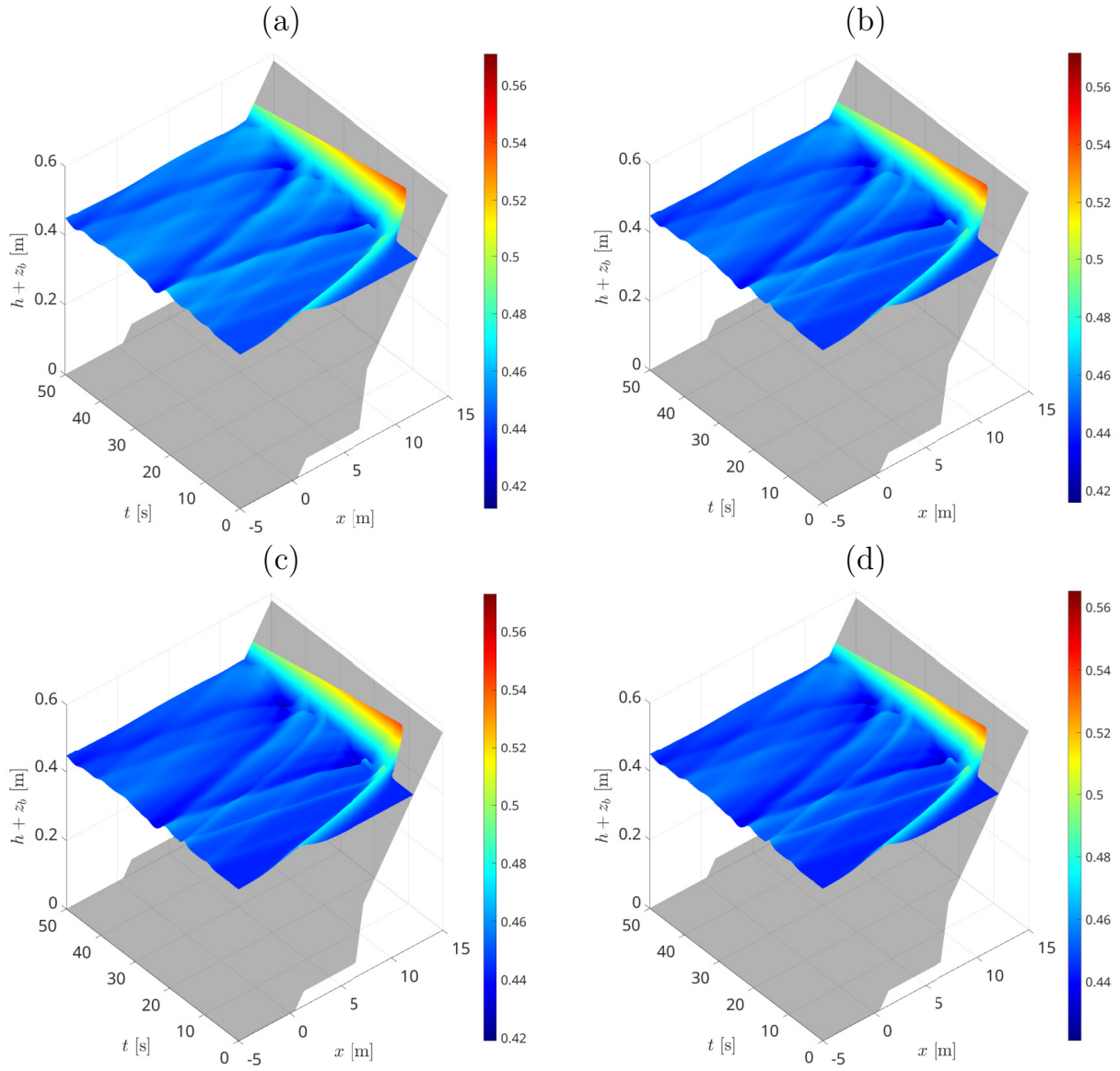

FIGURE 7. Numerical simulations of (a) Case 1, (b) Case 3, (c) Case 5 and (d) Case 13.

left of x_8), $C_{\mathrm{D}}(x_{8,\mathrm{b}})$ which is the drag coefficient of the "back part" (to the right of x_8), and $C_{\mathrm{D}}(x_9)$. Also, the position of $x_{8,\mathrm{f}}$ changes for each case. For Cases 1 to 5 is located in the middle of the vegetation area, whereas that for Cases 6 to 13, $x_{8,\mathrm{f}}$ is located in the interface where the vegetation structure changes. In Case 8, these four values that determine C_{D} are 0.83, 1.07, 0.84, and 0.74, and the corresponding tree densities of the front and back part are given by (43) with $d_n = 115.5$ and $W = W_{\mathrm{f}}$ and $W = W_{\mathrm{b}}$, respectively, giving $n_{\mathrm{t}} = n_{\mathrm{t,f}} = 3609.4\,\mathrm{m}^{-2}$ and $n_{\mathrm{t}} = n_{\mathrm{t,b}} = 902.3\,\mathrm{m}^{-2}$ for the tree densities in the front and back parts, respectively; see Figure 6 (d) for the experimental data. Finally, Case 13 is composed of the same patches of vegetation as Case 8 but the front and back parts are reversed; now C_{D} results from piecewise linear interpolation of

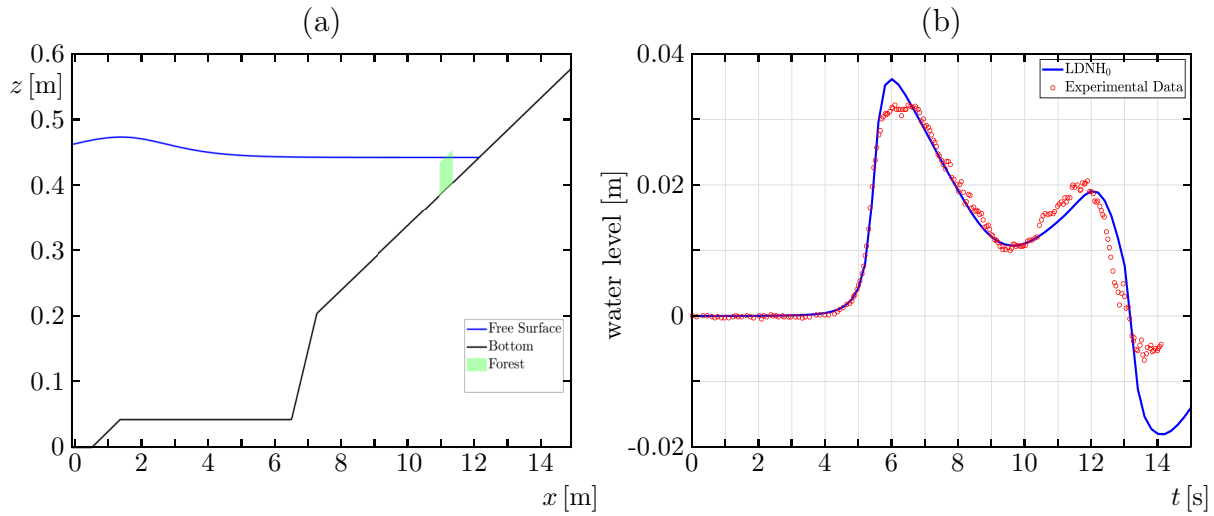

FIGURE 8. Examples 2 to 6: (a) initial condition of the simulation, (b) Example 3 [19, Case 3]: temporal evolution at $x = 11.36\,\mathrm{m}$ compared with experimental data.

$C_{\mathrm{D}}(x_7) = 0.76$, $C_{\mathrm{D}}(x_{8,\mathrm{f}}) = 0.76$, $C_{\mathrm{D}}(x_{8,\mathrm{b}}) = 0.92$ and $C_{\mathrm{D}}(x_9) = 1.26$, and we get $n_{\mathrm{t}} = n_{\mathrm{t,f}} = 902.3\,\mathrm{m}^{-2}$ and $n_{\mathrm{t}} = n_{\mathrm{t,b}} = 3609.4\,\mathrm{m}^{-2}$.

On the other hand, in [18], the authors analyse and compare of different approaches for describing and generating solitary waves by plates in a flume. We found that the profile that best matched the initial condition was the solution found by Rayleigh [23] that is given by

$$\eta(x) = \eta_0 \mathrm{sech}^2\left(\beta x\right), \qquad \text{with} \qquad \beta = \sqrt{\frac{3\eta_0}{4h_0^2(h_0+\eta_0)}}, \tag{44}$$

where η_0 is the wave amplitude and h_0 height of water. This means that the wave velocity is

$$u(x) = c\frac{\eta}{h}, \qquad \text{with} \qquad c = \sqrt{g(h_0+\eta_0)}.$$

In order to fit the wave into the channel we slightly extend the computational domain to $x < 0$.

In addition to the experimental data we include in Figure 7 numerical simulations of the water level over time. All numerical simulations for Examples 2 to 16 have been obtained with $\Delta x = 0.02\,\mathrm{m}$ and are based on a CFL number of 0.8. The simulations of Examples 2 to 6 in Figure 6 have been obtained by the LDNH_0. For Case 3 of [19] (our Example 3) we also display in Figure 8 (b) the simulated water height at $x = x_9 = 11.36\,\mathrm{m}$, the position of G_9, as a function of time.

5.3. **Examples 7 to 10: Iimura-Tanaka experiment and LDNH_0 multi-layer tests.**

Having calibrated the model using the experimental data, we are now ready to simulate diverse scenarios that account for trees with properties that vary along the vertical axis. We use the same initial condition as for Examples 2 to 6. All simulations employ the same initial condition for the water waves, namely the one given by (44).

Now the vegetation parameters depend on height z. Equation (42) is replaced by

$$d_{n,\alpha} = \frac{2}{\sqrt{3}D_{\mathrm{f}}^2} W_{\mathrm{f}} \bar{d}_\alpha \times 10^5 + \frac{2}{\sqrt{3}D_{\mathrm{b}}^2} W_{\mathrm{b}} \bar{d}_\alpha \times 10^5, \quad \alpha = 1, \ldots, N,$$

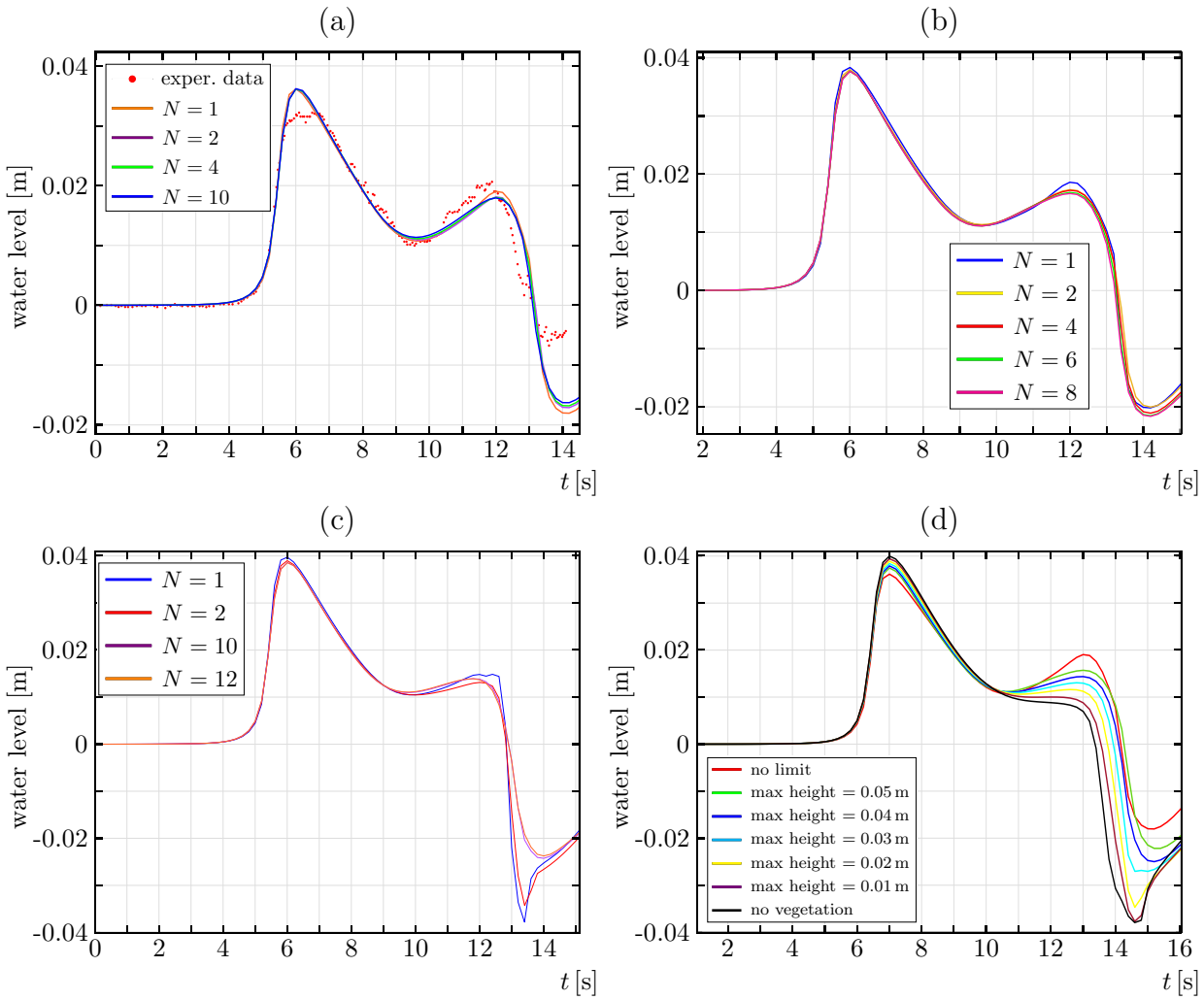

FIGURE 9. Examples 7 to 10: simulated water levels at $x = 11.36\,\mathrm{m}$ for variants of [19, Case 3]: (a) Example 7: simulation based on data of Example 2 but performed with various numbers of layers N, (b) Example 8: simulations with tree height limited to 0.05 m (via (45)) performed with various numbers of layers N, (c) Example 9: analogous result for maximum tree height 0.03 m. (d) Example 10: water levels for various maximum heights of vegetation for $N = 10$ layers.

that is we assume that d_n is specific for each layer α. The average tree diameter $\bar{d}_\alpha$ is defined in (33). On the other hand, D_f and D_b are calculated from the centers of the trees and we assume trees have layer-wise cylindrical symmetry so they do not change with respect to ζ. Likewise, W_f and W_b do not depend on ζ or z either. Furthermore, to include the effects of branches and leaves given by $c_\mathrm{tr}(\zeta)c_\mathrm{le}(\zeta)$ (see Section 3.5) one usually defines

$$d_{n,\mathrm{all}} \coloneqq d_n \times c_\mathrm{tr} c_\mathrm{le}.$$

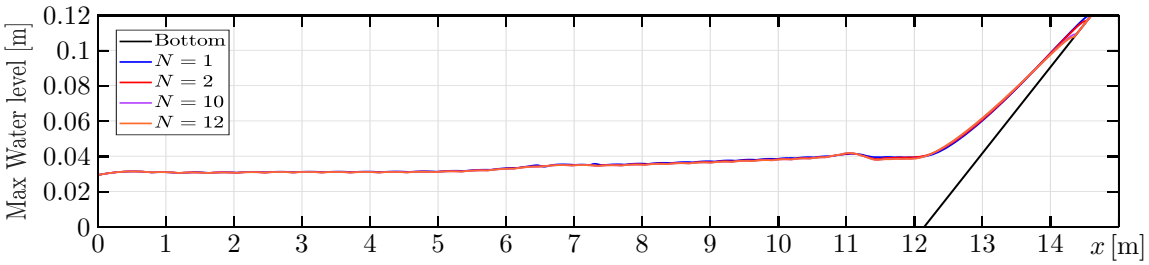

FIGURE 10. Example 9: maximum water level for maximum vegetation height 0.03m obtained for various numbers of layers N.

For the multilayer model we generalize this as

$$d_{n,\mathrm{all},\alpha} = d_{n,\alpha} \times (\overline{c_{\mathrm{tr}} c_{\mathrm{le}}})_\alpha, \quad \alpha = 1, \ldots, N.$$

In Example 7 we simulate again [19, Case 3], as in Example 2. We utilize exactly the same (non-layer-specific) parameters as in Example 2, i.e., the properties of vegetation are constant with respect to z. The purpose of this example is to elucidate that when the parameters of vegetation do not depend on the vertical coordinate z then the numerical solution only depends marginally on the number N of layers, as can be seen in Figure 9 (a).

Next, we proceed to investigate the impact of varying tree heights. In Example 8 we assume that the trees have a height of 0.05 m (measured from ground). This information is incorporated by setting

$$d(\zeta) = \begin{cases} 0.05\,\mathrm{m} & \text{for } \zeta < 0.05\,\mathrm{m}, \\ 0\,\mathrm{m} & \text{for } \zeta \geq 0.05\,\mathrm{m}. \end{cases} \tag{45}$$

The corresponding numerical result is shown in Figure 9 (b). The result is nearly the same for all numbers of layers considered, most likely because the wave is too small to pass over the vegetation. However, if it is assumed that all trees have maximum height 0.03 m, then differences in the numerical solution in dependence of the number of layers do become visible (Example 9, see Figure 9 (c)). In the latter case, the simulated maximum water level (at each position, taken over time) shown in Figure 10 does not exhibit major differences with respect to the number of layers N; the maximum run-up height does, hoever, slightly vary with N (see the situation near $x = 14\,\mathrm{m}$).

Finally, Example 10 (see Figure 9 (d)) shows how the water level, simulated with $N = 10$ layers, depends on the height of trees that varies between 0 m (no vegetation at all) to the unlimited case. Note that the numerical solutions corresponding to each of the seven cases are ordered consistently, and that while the cases with no vegetation or small tree height cause slightly higher water levels around $t = 7\,\mathrm{s}$, the returning wave produces a marked extremum around $t = 13\,\mathrm{s}$ for the unlimited tree height or when the tree height is 0.05 m or 0.04 m. This property alerts to the accumulation of water behind the forest when the wave returns.

5.4. **Examples 11 to 15: simulations with height-dependent tree properties**

As the case of Experiment 7 showed, utilizing a multilayer scheme instead of a single-layer approach does not produce significantly new results when the vegetation is vertically homogeneous. However, when the vegetation has properties that strongly vary with height then results significantly depend on the number of layers. To illustrate this point we consider a vegetation area of trees for which the parameter $c_{\mathrm{tr}} c_{\mathrm{le}}(z)$ (see Section 3.5) varies with height z. To this end we fit a polynomial to the experimental data.

We utilize information by Tanaka et al. [29] who estimated the product $(c_{\mathrm{tr}} c_{\mathrm{le}})(\zeta)$ for a number of tree species that are representative of the coastal vegetation affected by the Indian Ocean tsunami of 26 December 2004.

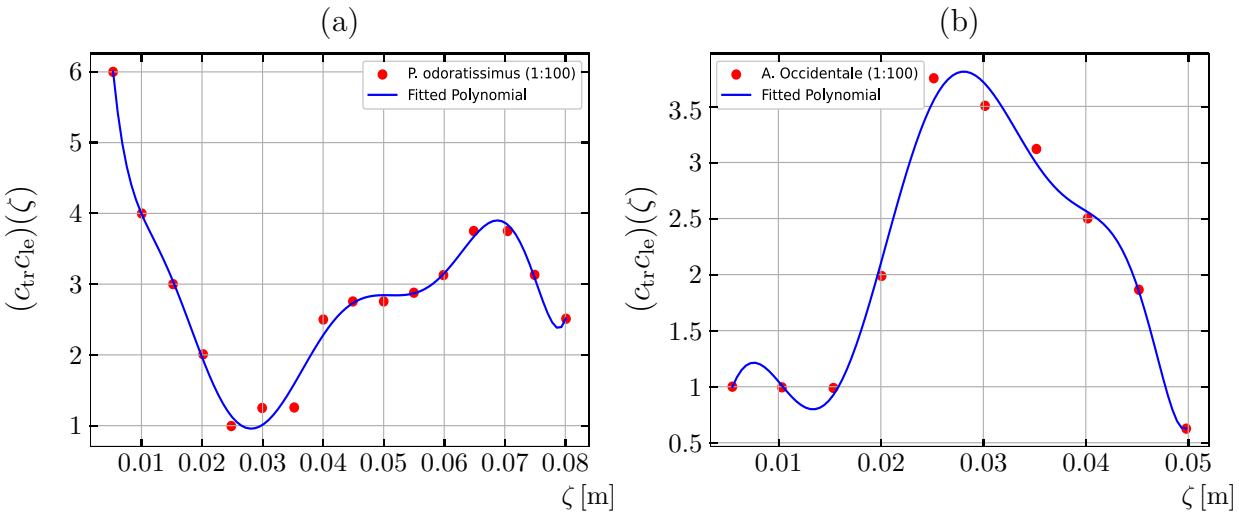

FIGURE 11. Examples 11 to 16: approximation of experimental information from [29] on $(c_{\mathrm{tr}}c_{\mathrm{le}})(\zeta)$, scaled to 1/100, by fitting polynomials of degree 8 to data of (a) *P. Odoratissimus*, (b) *A. Occidentale*. Note that ζ measures height along one tree from ground.

(This combination is denoted $\alpha(z)\beta(z)$ in [29].) Two of these species, *Pandanus odoratissumus*, a representative tree that grows in beach sand, and *Anarcadium occidentale*, a plantation species in the coastal zone of Sri Lanka and the Andaman coast of Thailand, are selected here because their properties change appreciably along the vertical axis (see [29] for detailed information). Figure 9 of [29] displays empirical information on the vertical distribution of $(c_{\mathrm{tr}}c_{\mathrm{le}})(z)$ for these (and other) species. We have used this information, scaled by 1/100, to provide this function in both cases after fitting the measured values to a polynomial of suitable degree (Figure 11).

Examples 11 and 12 are based on [19, Case 3], as are Examples 2 and 7 to 10, but we now utilize the function tree properties that depend on z as described by the function $(c_{\mathrm{tr}}c_{\mathrm{le}})(z)$ corresponding to *P. Odoratissimus*. Figure 12 (a) displays the differences in the numerical solution coming from the use of various numbers of layers N. The results obtained by $N = 1$ layer and more layers are almost are indistinguishable. The likely reason for this behaviour is that the amplitude of the soliton is too small to produce appreciable vertical changes. In Figure 12 (b) we simulate the same scenario but this time the soliton has an amplitude of $h_0 = 0.0628\,\mathrm{m}$, that is the double of the original test. This time we obtain significant differences between the single-layer and the multi-layer model. In particular, $N = 4$ layers provide a satisfactory level of precision while also being significantly less computationally demanding compared to the model with $N = 10$ layers. In general results with more than four layers are almost identical. This observation is supported by Figure 13 where we consider again Example 12 but now measure the maximal water level for various values of N.

Results are slightly different if instead of *P. Odoratissimus* we consider the species *A. Occidentale*, for which significant differences are observed between using a single layer and multiple layers, as depicted in Figures 14 (a) and (b). The model with only one layer tends to overestimate the maximum wave height while underestimating the minimum water level. However, it is notable that using four layers once again proves to be sufficient in accurately modeling the situation. For Example 13 we also plot (in Figure 15 (a)) the simulated maximum water level for various numbers of layers. In particular in the vegetation zone (see Figure 15 (b)) differences between models with one layer and two or more layers become significant.

It is also possible to combine zones of vegetation with two distinct types of vegetation. Example 15 is similar to the arrangement of [19, Case 13] but we now assume that the vegetation of the front part (see Figure 5) consists of *P. Odoratissimus* and the back part of *A. Occidentale*, see Figure 16.

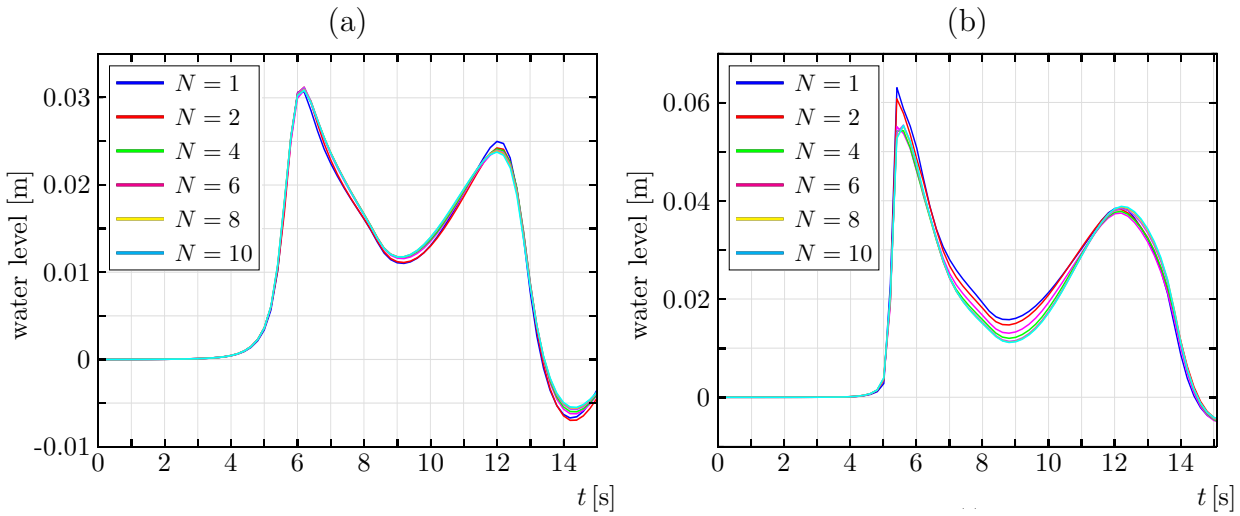

FIGURE 12. Examples 11 and 12: simulated water levels observed at $x = 11.36\,\mathrm{m}$ with $(c_{\mathrm{tr}}c_{\mathrm{le}})(z)$ corresponding to *P. Odoratissimus*, trees of height 0.08 m, and various numbers of layers N: (a) with a soliton amplitude $h_0 = 0.0314\,\mathrm{m}$ (Example 11), (a) with a soliton amplitude $h_0 = 0.0628\,\mathrm{m}$ (Example 12).

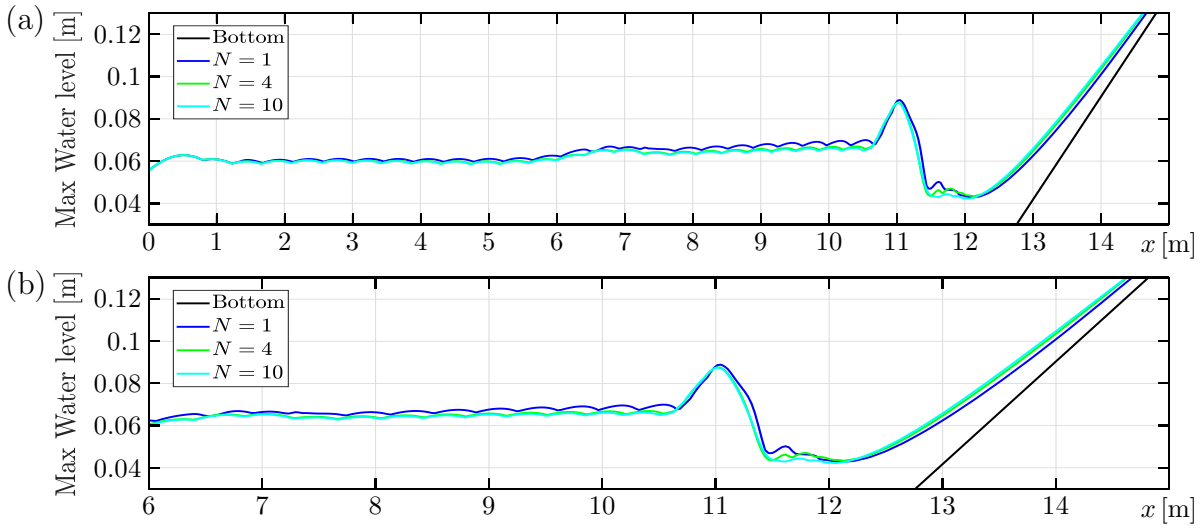

FIGURE 13. Example 12: (a) maximum water levels for various numbers of layers N, (b) enlarged view of (a).

5.5. **Example 16: simulations with drag dependent on a Reynolds number**

Rodríguez et al. [24] estimate the drag coefficient for for two Chilean native trees, *Pinus Radiata* and *Cupressus Macrocarpa*. In the article the authors calculate the drag coefficient, including the vertical structure as

$$C_{\text{d-all}} = c_{\mathrm{tr}}c_{\mathrm{le}} \times C_{\mathrm{D}}, \tag{46}$$

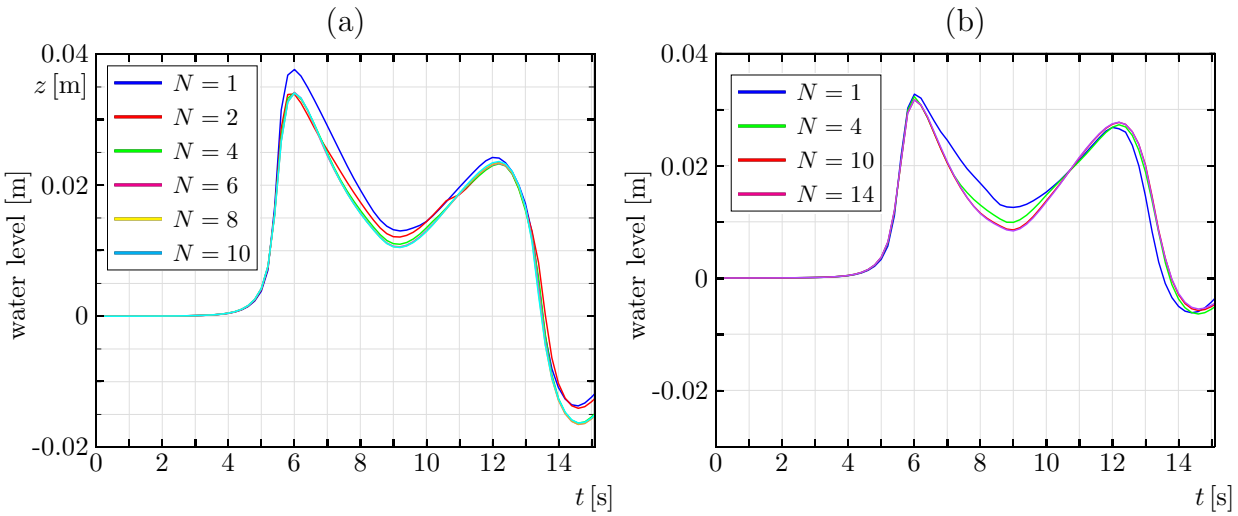

FIGURE 14. Examples 13 and 14: simulated water levels measured at $x = 11.36\,\mathrm{m}$ for various numbers of layers for a vegetation of *A. Occidentale* with a tree height of 0.05 m and a distribution of vegetation according to (a) [19, Case 3] (Example 13), (b) [19, Case 13] (Example 14).

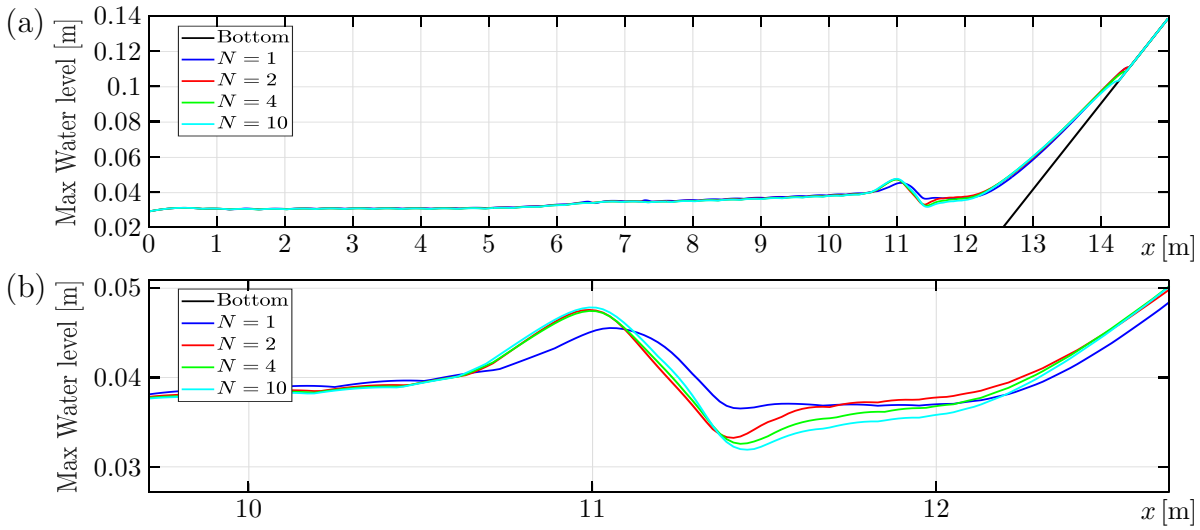

FIGURE 15. Example 13: (a) maximum water levels for various numbers of layers for a vegetation of *A. Occidentale* with a tree height of 0.05 m and a distribution of vegetation according to [19, Case 3], (b) enlarged view of (a).

where the expression

$$C_{\mathrm{D}}(\mathrm{Re}) = \begin{cases} 1.2 & \text{if } \mathrm{Re} \le 2 \times 10^5, \\ 1.2 - 0.5\left(\dfrac{\mathrm{Re}}{3 \times 10^5} - \dfrac{2}{3}\right) & \text{if } 2 \times 10^5 \le \mathrm{Re} \le 5 \times 10^5, \\ 0.7 & \text{if } \mathrm{Re} \ge 5 \times 10^5. \end{cases}$$

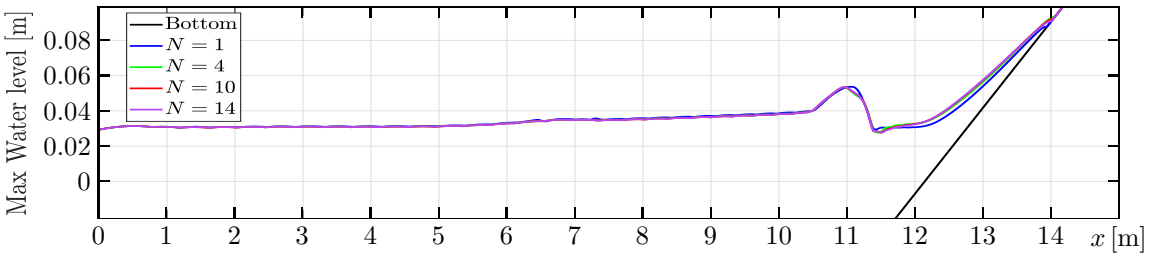

FIGURE 16. Example 15: maximum water levels for various numbers of layers using a distribution of vegetation following [19, Case 13] with *P. Odoratassimus* and *A. Occidentale* in the front and back parts, respectively.

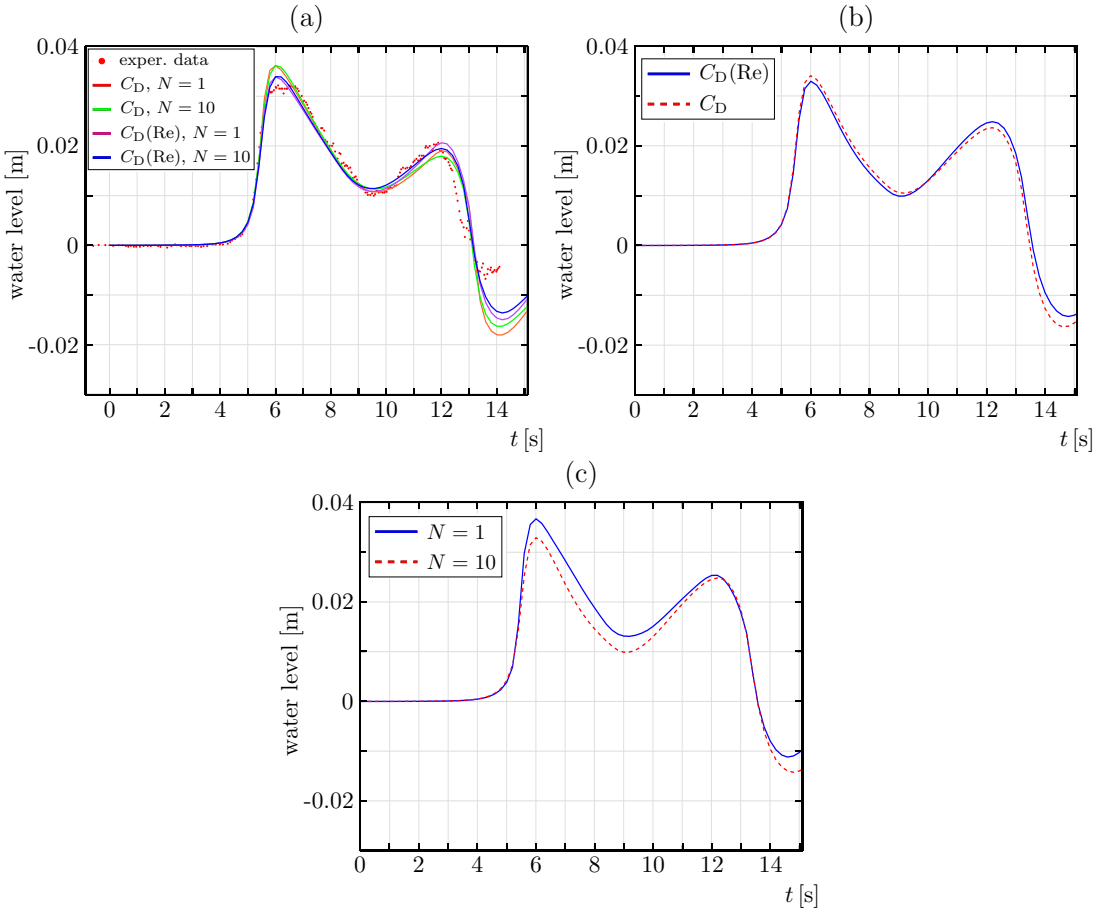

FIGURE 17. Example 16: comparison between the drag calculated by [19] and the Reynolds number dependent dependent drag $C_D(\mathrm{Re}_\alpha)$ for various numbers of layers: (a) Case 3 at $x = 11.36\,\mathrm{m}$. (b) Case 3 at $x = 11.36\,\mathrm{m}$ using *A. Occidentale* with one layer. (c) Case 3 at $x = 11.36\,\mathrm{m}$ with *A. Occidentale* and $C_D(\mathrm{Re}_\alpha)$ for various numbers of layers.

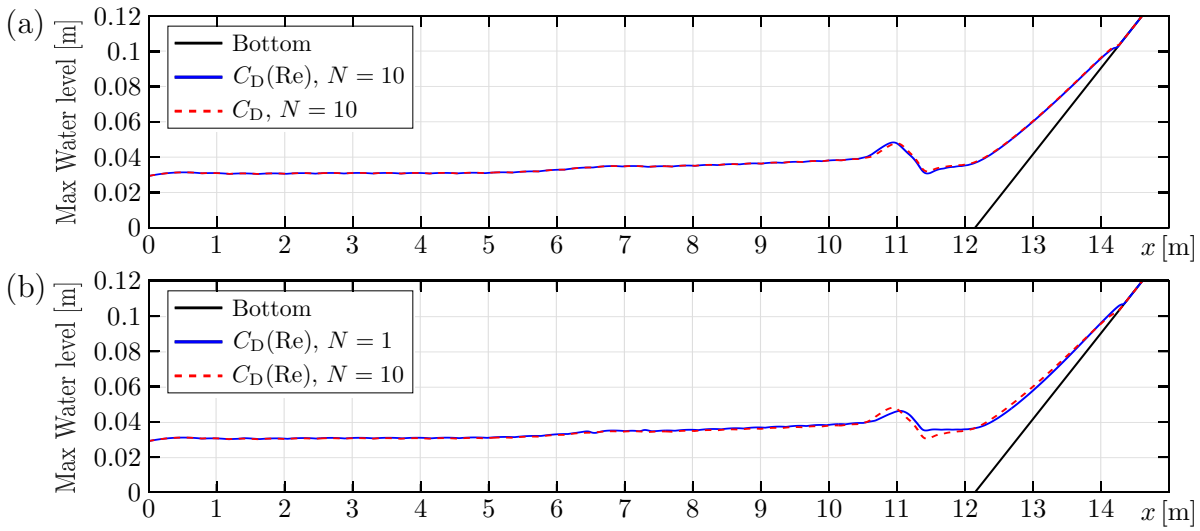

FIGURE 18. Example 16: comparison of the maximum water level for one and ten layers using various drag coeffcients: (a) and (b) Case 3 using *A. Occidentale.*

used in [32] is employed. Here $\mathrm{Re} = d_z|u|/\nu_{\mathrm{water}}$ is the Reynolds number, where d_z the diameter of the stem and ν_{water} the kinematic viscosity of water. To implement this approach within the multilayer model, we use that each layer has it own Reynolds number given by $\mathrm{Re}_\alpha = \bar{d}_\alpha|u_\alpha|/\nu_{\mathrm{water}}$. In Example 16 we illustrate how to incorporate this model of the drag into the multilayer model by calculating the drag coefficient for each layer using its own Reynolds number, denoted as Re_α, see Figures 17 and 18.

6. Conclusions

In this research, we have successfully modeled tsunamis and explored the potential of coastal vegetation as a means of mitigation. By employing finite volume methods combined with projection methods for non-hydrostatic pressure, we have accurately simulated tsunami propagation. The study's validation using experimental observations strengthens the reliability of our findings.

Through the development of a multilayer system model based on LDNH_0, we have surpassed the limitations of current vegetation models. Unlike traditional Boussinesq-like models that rely solely on average values of vegetation properties, our multilayer approach takes into account the vertical variability within the forest. By incorporating vertical dependency into the drag forces, inertia forces, and porosity, we have extended the model to accurately capture the precise properties and behavior of coastal vegetation.

Our investigation into the influence of forest properties on model performance reveals valuable insights. In scenarios where the forest properties, such as the diameter and drag coefficient of trees, remain constant along the vertical axis, the addition of more layers to the system does not yield significant improvements when compared to the experimental data. Therefore, for such scenarios, a single layer is sufficient. However, in cases where the vegetation properties, such as the diameter and drag coefficient, vary along the vertical axis, a single layer is inadequate for modeling the system, and the addition of more layers is expected to yield better results.

The findings of this study highlight the potential of our multilayer system model by demonstrating significant percentage differences when compared to the traditional method that relies on average vegetation properties. For example, for *P. Odoratissimus* vegetation, our model shows percentage differences of up to 29%, while for *A. Occidentale*, the differences reach approximately 10%. This substantial improvement in accuracy emphasizes the importance of our new approach and its ability to provide more precise results.

These findings contribute to the understanding of the complex interactions between tsunamis and coastal vegetation, shedding light on the importance of incorporating vertical variability in vegetation models. By utilizing our multilayer approach, researchers and decision-makers can make more informed assessments of the effectiveness of coastal vegetation as a natural defense against tsunamis and develop targeted strategies for coastal planning and management.

Further research is warranted to explore additional factors and refine the parameters of our multilayer system model. By expanding our knowledge in this area, we can continue to enhance the accuracy and applicability of our approach, further improving our understanding of coastal hazards and strengthening our ability to mitigate their impact.

Appendix A. LDNH$_0$ soliton

We assume a flat bottom ($z = \text{const.}$) and assume that the variables do not depend on x and t independently but rather on $\xi = x - ct$, with a constant c to be determined. Inserting this approach into (10) we get

$$u = c + \frac{\gamma}{h},$$

where γ is a constant that can be determined by considering a region where the wave has already passed and is now at rest. In such a region the speed u is zero, hence γ must be given by $\gamma = -ch_0$, where h_0 is the still water height. On the other hand, taking into account that

$$\partial_t(hu) = -c^2\partial_\xi h \quad \text{and} \quad \partial_x(hu^2) = c^2\partial_\xi h - \frac{\gamma^2}{h^2}\partial_\xi h = c^2\partial_\xi h + \gamma^2\partial_\xi\left(\frac{1}{h}\right),$$

we obtain

$$\partial_t(hu) + \partial_x(hu^2) = \gamma^2\partial_\xi\left(\frac{1}{h}\right),$$

hence integrating the linear momentum equation (10b) we obtain

$$p(z) = \frac{A}{h(\xi)} - \frac{\gamma^2}{h^2(\xi)} - \frac{gh(\xi)}{2},$$

where A is a constant of integration that can be evaluated in the same way as γ. The result is $A = gh_0\left(3h_0 + 2\eta_0\right)/2$, with η_0 the amplitude of the wave. Finally, using the constraint (10d) we may evaluate w:

$$w = -\frac{h}{2}\partial_x u.$$

Furthermore, assume that $h(\xi) = h_0 + \eta_0\,\mathrm{sech}^2(\beta\xi)$ with a constant β to be determined. Then $h(\xi)$ satisfies

$$h' = -2\beta(h - h_0)\sqrt{1 - \frac{h - h_0}{\eta_0}}.$$

Inserting all these expressions into (10c) we end up with the equation

$$-\frac{2A}{h(\xi)} - \frac{2h_0^3\gamma^2\beta^2}{\eta_0 h^2(\xi)} - \frac{2h_0^2\gamma^2\beta^2}{h^2(\xi)} + \frac{3h_0^2\gamma^2\beta^2}{\eta_0 h(\xi)} + \frac{2h_0\gamma^2\beta^2}{h(\xi)} - \frac{\gamma^2\beta^2 h(\xi)}{\eta_0} + \frac{2\gamma^2}{h^2(\xi)} + gh(\xi) = 0.$$

This is a cubic equation can be seen as a cubic polynomial for h where the only thing left is the value of β , solving this equation we find that

$$\beta = \sqrt{\frac{\eta_0}{h_0^2\,(h_0+\eta_0)}} \quad \text{and} \quad c = \sqrt{g(h_0+\eta_0)}.$$

Writing again (x,t) instead of ξ we obtain the soliton solution

$$\begin{aligned} h(x,t) &= h_0 + \eta_0 \mathrm{sech}^2\left(\beta(x-ct)\right), \\ u(x,t) &= c\left(1-\frac{h_0}{h}\right), \\ w(x,t) &= \frac{c\beta h_0 \tanh(\beta(x-ct))\,(h-h_0)}{h}, \\ p(x,t) &= \frac{gh_0\,(3h_0+2\eta_0)}{2h} - \frac{(h_0 c)^2}{h^2} - \frac{gh}{2}, \end{aligned} \tag{A.1}$$

see Figure 19. In particular, here we showed a simple way to find this soliton because we knew the functional

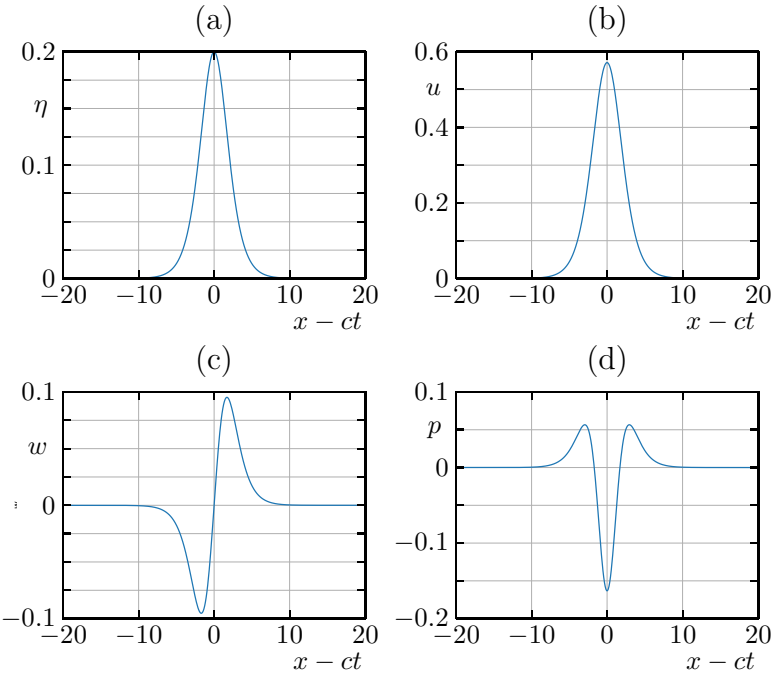

FIGURE 19. Graphs of LDNH_0 soliton solution with $h_0 = 1$ and $\eta_0 = 0.2$.

form of $h(\xi)$ and it is easy to verify that this is solution of (10), but in order to find $h(\xi)$ we did use the sech method, and more complex models will require full use of it.

REFERENCES

[1] E. Audusse, A multilayer Saint-Venant model: derivation and numerical validation. *Discrete Contin. Dyn. Syst. Ser. B* **5** (2005) 189–214.

[2] E. Audusse and M.-O. Bristeau, Finite-volume solvers for a multilayer Saint-Venant system. *Int. J. Appl. Math. Comput. Sci.* **17** (2007) 311–319.

[3] E. Audusse, M.-O. Bristeau and A. Decoene, Numerical simulations of 3D free surface flows by a multilayer Saint-Venant model. *Int. J. Numer. Methods Fluids* **56** (2008) 331–350.

[4] E. Audusse, M. Bristeau, B. Perthame and J. Sainte-Marie, A multilayer Saint-Venant system with mass exchanges for shallow water flows. Derivation and numerical validation. *ESAIM: Math. Model. Numer. Anal.* **45** (2011) 169–200.

[5] E. Audusse, M.-O. Bristeau, M. Pelanti and J. Sainte-Marie, Approximation of the hydrostatic Navier–Stokes system for density stratified flows by a multilayer model: kinetic interpretation and numerical solution. *J. Comput. Phys.* **230** (2011) 3453–3478.

[6] R. Bürger, E.D. Fernández-Nieto and V. Osores, A dynamic multilayer shallow water model for polydisperse sedimentation. *ESAIM: Math. Model. Numer. Anal.* **53** (2019) 1391–1432.

[7] R. Bürger, E.D. Fernández-Nieto and V. Osores, A multilayer shallow water approach for polydisperse sedimentation with sediment compressibility and mixture viscosity. *J. Sci. Comput.* **85** (2020), article 49 (40pp).

[8] M. J. Castro and E. Fernández-Nieto, A class of computationally fast first order finite volume solvers: PVM methods. *SIAM J. Sci. Comput.* **34** (2012) A2173–A2196.

[9] M. J. Castro, A. M. Ferreiro Ferreiro, J. A. García-Rodríguez, J. M. González-Vida, J. Macías, C. Parés and M. E. Vázquez-Cendón, The numerical treatment of wet/dry fronts in shallow flows: application to one-layer and two-layer systems. *Math. Comput. Modelling* **42** (2005) 419–439.

[10] M. J. Castro Díaz, J. Gallardo and C. Parés, High order finite volume schemes based on reconstruction of states for solving hyperbolic systems with nonconservative products. Applications to shallow-water systems. *Math. Comput.* **75** (2006) 1103–1134.

[11] M. J. Castro, T. Morales de Luna and C. Parés, Well-balanced schemes and path-conservative numerical methods. Chapter 6 in R. Abgrall and C.-W. Shu (eds.), Handbook of Numerical Methods for Hyperbolic Problems: Applied and Modern Issues. Handbook of Numerical Analysis vol. 18, Elsevier/North Holland, Amsterdam, 2017, 131–175.

[12] G. Dal Maso, P. G. LeFloch and F. Murat, Definition and weak stability of nonconservative products. *J. Math. Pures Appl.* **74** (1995) 483–548.

[13] C. Escalante Sánchez, E. D. Fernández-Nieto, T. Morales de Luna, Y. Penel and J. Sainte-Marie, Numerical simulations of a dispersive model approximating free-surface Euler equations. *J. Sci. Comput.* **89** (2021) article 55 (32pp).

[14] E. D. Fernández-Nieto, E. H. Koné and T. Chacón Rebollo, A multilayer method for the hydrostatic Navier–Stokes equations: a particular weak solution. *J. Sci. Comput.* **60** (2014) 408–437.

[15] E. Fernández-Nieto, J. Garres-Díaz, A. Mangeney and G. Narbona-Reina, A multilayer shallow model for dry granular flows with the $\mu(I)$-rheology: Application to granular collapse on erodible beds. *J. Fluid Mech.* **798** (2016) 643–681.

[16] E. D. Fernández-Nieto, E. H. Koné, T. Morales de Luna and R. Bürger, A multilayer shallow water system for polydisperse sedimentation. *J. Comput. Phys.* **238** (2013) 281–314.

[17] E. D. Fernández-Nieto, M. Parisot, Y. Penel and J. Sainte-Marie, A hierarchy of dispersive layer-averaged approximations of Euler equations for free surface flows, *Commun. Math. Sci.* **16** (2018) 1169–1202.

[18] K. Guizien and E. Barthélemy, Accuracy of solitary wave generation by a piston wave maker, *J. Hydraul. Res.* **40** (2002) 321–331.

[19] K. Iimura and N. Tanaka, Numerical simulation estimating effects of tree density distribution in coastal forest on tsunami mitigation. *Ocean Engrg.* **54** (2012) 223–232.

[20] A. Kurganov and G. Petrova, A second-order well-balanced positivity preserving central-upwind scheme for the Saint-Venant system. *Commun. Math. Sci.* **5** (2007) 133–160.

[21] C. Parés, Numerical methods for nonconservative hyperbolic systems: a theoretical framework. *SIAM J. Numer. Anal.* **44** (2006) 300–321.

[22] C. Parés and M. J. Castro, On the well-balance property of Roe's method for nonconservative hyperbolic systems. Applications to shallow-water systems. *M2AN Math. Model. Numer. Anal.* **38** (2004) 821–852.

[23] Rayleigh, Lord (J. W. Strutt), On waves. *Phil. Mag. (5)* **1** (1876) 257–279.

[24] R. Rodríguez, P. Encina, M. Espinosa and N. Tanaka, Field study on planted forest structures and their role in protecting communities against tsunamis: experiences along the coast of the Biobío Region, Chile. *Landscape Ecol. Eng.* **12** (2016) 1–12.

[25] P. L. Roe, Approximate Riemann solvers, parameter vectors, and difference schemes. *J. Comput. Phys.* **43** (1981) 357–372.

[26] J. Sainte-Marie, Vertically averaged models for the free surface non-hydrostatic Euler system: derivation and kinetic interpretation. *Math. Models Methods Appl. Sci.* **21** (2011) 459–490.

[27] C. E. Sánchez, E. D. Fernández-Nieto, T. Morales de Luna, Y. Penel and J. Sainte-Marie, Numerical simulations of a dispersive model approximating free-surface Euler Equations. *J. Sci. Comput.* **89** (2021) article 55.

[28] N. Shuto, The effectiveness and limit of tsunami control forests. *Coastal Engrg. Japan* **30** (1987) 143–153.

[29] N. Tanaka, Y. Sasaki, M. I. M. Mowjood, K. B. S. N. Jinadasa and S. Homchuen, Coastal vegetation structures and their functions in tsunami protection: Experience of the recent Indian Ocean tsunami. *Landscape Ecol. Eng.* **3** (2007) 33–45.

[30] N. Tanaka, Effectiveness and limitations of vegetation bioshield in coast for tsunami disaster mitigation. Chapter 9 in N.-A. Mörner (ed.), The Tsunami Threat — Research and Technology, InTech, Rijeka, Croatia, 2011, 161–178.

[31] I. Toumi, A weak formulation of Roe's approximate Riemann solver. *J. Comput. Phys.* **102** (1992) 360–373.
[32] H. Yanagisawa, S. Koshimura, K. Goto, T. Miyagi, F. Imamura, A. Ruangrassamee and C. Tanavud, The reduction effects of mangrove forest on a tsunami based on field surveys at Pakarang Cape, Thailand and numerical analysis. *Estuar. Coast. Shelf Sci.* **81** (2009) 27–37.

Centro de Investigación en Ingeniería Matemática (CI^{2}MA)

PRE-PUBLICACIONES 2023 - 2024

2023-27 Raimund Bürger, Yessennia Martínez, Luis M. Villada: *Front tracking and parameter identification for a conservation law with a space-dependent coefficient modeling granular segregation*

2023-28 Marie Haghebaert, Beatrice Laroche, Mauricio Sepúlveda: *Study of the numerical method for an inverse problem of a simplified intestinal crypt*

2023-29 Rodolfo Araya, Fabrice Jaillet, Diego Paredes, Frederic Valentin: *Generalizing the Multiscale Hybrid-Mixed Method for Reactive-Advective-Diffusive Equations*

2023-30 Jessika Camaño, Ricardo Oyarzúa, Miguel Serón, Manuel Solano: *A mass conservative finite element method for a nonisothermal Navier-Stokes/Darcy coupled system*

2023-31 Franz Chouly, Hao Huang, Nicolás Pignet: *HHT-α and TR-BDF2 schemes for Nitsche-based discrete dynamic contact*

2024-01 Sergio Caucao, Gabriel N. Gatica, Saulo Medrado, Yuri D. Sobral: *Nonlinear twofold saddle point-based mixed finite element methods for a regularized $\mu(I)$-rheology model of granular materials*

2024-02 Julio Careaga, Gabriel N. Gatica, Cristian Inzunza, Ricardo Ruiz-Baier: *New Banach spaces-based mixed finite element methods for the coupled poroelasticity and heat equations*

2024-03 Harold D. Contreras, Paola Goatin, Luis M. Villada: *A two-lane bidirectional nonlocal traffic model*

2024-04 Rommel Bustinza, Matteo Cicuttin, Ariel Lombardi: *A Hybrid High-Order method for the mixed Steklov eigenvalue problem*

2024-05 Isaac Bermudez, Jaime Manríquez, Manuel Solano: *A hybridizable discontinuous Galerkin method for Stokes/Darcy coupling in dissimilar meshes*

2024-06 Thomas Führer, Diego Paredes: *Robust hybrid finite element methods for reaction-dominated diffusion problems*

2024-07 Raimund Bürger, Enrique D. Fernández Nieto, Jorge Moya: *A multilayer shallow water model for tsunamis and coastal forest interaction*

Para obtener copias de las Pre-Publicaciones, escribir o llamar a: Director, Centro de Investigación en Ingeniería Matemática, Universidad de Concepción, Casilla 160-C, Concepción, Chile, Tel.: 41-2661324, o bien, visitar la página web del centro: http://www.ci2ma.udec.cl







Centro de Investigación en
Ingeniería Matemática (CI²MA)
Universidad de Concepción

Casilla 160-C, Concepción, Chile
Tel.: 56-41-2661324/2661554/2661316
http://www.ci2ma.udec.cl